

Optical, vibrational, thermal, electrical, damage and phase-matching properties of lithium thioindate

S. Fossier, S. Salaiün, J. Mangin and O. Bidault

Laboratoire de Physique de l'Université de Bourgogne (UMR-CNRS 5027), 9 avenue A. Savary, F-21078 Dijon, France.

I. Thénot and J.-J. Zondy*

*BNM-SYRTE, Observatoire de Paris (UMR-CNRS 8630),
61 avenue de l'Observatoire, F-75014 Paris, France.*

W. Chen

*Laboratoire de Physicochimie de l'Atmosphère (UMR-CNRS 8101),
Université du Littoral Côte d'Opale, 145 Av. Maurice Schumann, F-59140 Dunkerque, France.*

F. Rotermund† and V. Petrov

Max-Born Institute for Nonlinear Optics and Ultrafast Spectroscopy, 2A Max-Born St, D-12489 Berlin, Germany.

P. Petrov and J. Henningsen

Danish Institute of Fundamental Metrology, B 307 Matematiktorvet, DK-2800, Lyngby, Denmark.

A. Yelissev, L. Isaenko and S. Lobanov

*Design and Technological Institute for Monocrystals SB-RAS,
43 Russkaya St, RU-630058, Novosibirsk, Russia.*

O. Balachninaite,‡ G. Slekyš,‡ and V. Sirutkaitis‡

Altechna Co. Ltd, Ukmerges 41A-203, LT-2004, Vilnius, Lithuania.

(Dated: August 1, 2018)

Lithium thioindate (LiInS_2) is a new nonlinear chalcogenide biaxial material transparent from 0.4 to 12 μm , that has been successfully grown in large sizes and good optical quality. We report on new physical properties that are relevant for laser and nonlinear optics applications. With respect to $\text{AgGaS}(\text{e})_2$ ternary chalcopyrite materials, LiInS_2 displays a nearly-isotropic thermal expansion behavior, a 5-times larger thermal conductivity associated with high optical damage thresholds, and an extremely low intensity-dependent absorption allowing direct high-power downconversion from the near-IR to the deep mid-IR. Continuous-wave difference-frequency generation (5–11 μm) of Ti:sapphire laser sources is reported for the first time.

PACS numbers: 42.70.Mp; 42.65.Ky, 42.65.Lm, 65.40.Ba, 65.40.De, 78.20.Fm, 78.20.Hp, 78.20.Jq, 78.20.Nv, 78.30.Fs, 61.80.Ba

I. INTRODUCTION

The intensive search for new nonlinear materials for the generation of coherent tunable radiation in the mid-IR (2 – 20 μm), a spectral range of importance for molecular spectroscopy, atmospheric sensing and various optoelectronic devices, remains a continuing challenge. In contrast with the oxides (with IR transmission range not exceeding $\sim 5 \mu\text{m}$) that attracted much attention lately, such deep mid-IR materials cannot be grown by well mastered hydrothermal, flux or Czochralski meth-

ods. Instead the more complex Bridgman-Stockbarger growth technique in sealed (high-pressure) ampoules, with volatile and chemically reactive starting components, is the only method used to produce large size single domain crystals, and this certainly hampered their development all the more that special post-growth treatments are needed to restore stoichiometry and improve their optical quality.

To date, only few suitable nonlinear crystals combining an extended transparency from the visible/near-IR to the deep mid-IR and large enough birefringence to allow phase-matching over the whole transparency range are available. The majority of these compounds belong to the ternary chalcogenide semi-conductors of the $\text{A}^{\text{I}}\text{B}^{\text{III}}\text{C}_2^{\text{VI}}$ family, where $\text{A}=\text{Cu}, \text{Ag}$; $\text{B}=\text{Al}, \text{Ga}, \text{In}$; $\text{C}=\text{S}, \text{Se}, \text{Te}$ [1]. Except for AgInS_2 , which can exist in both the tetragonal and orthorhombic phases [2], these crystallize in the chalcopyrite (CuFeS_2) structure with $I\bar{4}2d$ space group and tetragonal symmetry (class) $42m$ but only few of

*Electronic address: jean-jacques.zondy@obsppm.fr

†Present address: Department of Molecular Science and Technology, Ajou University, 5 Wonchun-dong, Paldal-gu, 442-749 Suwon, Korea

‡Also at: Laser Research Centre, Quantum Electronics Department, Vilnius University, LT-2040 Vilnius, Lithuania

them possess sufficient birefringence. Most of the commercially available nonlinear crystals (AgGaS₂ or AGS, AgGaSe₂ or AGSe, ZnGeP₂ or ZGP, GaSe, CdSe) or more confidential ones (HgGa₂S₄ or HGS, Ag₃AsS₃ or proustite, Tl₃AsSe₃ or TAS) have their advantages and drawbacks [3]. Despite their higher nonlinearity compared with the oxides, one limitation stems from their low energy bandgap, which prevents the use of pump lasers below 1 μm due to severe linear and two-photon absorption and associated thermal effects. ZGP has a high nonlinearity (72 pm/V) and thermal conductivity but requires pump wavelength above 2 μm due to its residual absorption in the near-IR. The noble metal compounds (AGS, AGSe) have the lowest residual absorption, but their poor thermal conductivity due to low-energy phonon spectrum limits their performance, especially in cw applications [4, 5, 6, 7]. Furthermore, their thermal expansion is anisotropic along the direction parallel and perpendicular to the optic axis, which is a source of thermo-mechanical stresses. CdSe's transparency extends up to 18 μm but its low birefringence and nonlinearity limit its phase-matching capability. GaSe is a soft, cleaving compound that cannot be cut at directions different from the optical axis, further its large birefringence results in severe walk-off limitations.

Two new materials belonging to the A^IB^{III}C₂^{VI} chalcogenide family, where the metal cations are replaced with the lighter alkali metal (A=Li), can now be added to this limited list: LiInS₂ or lithium thioindate (LIS) and LiInSe₂ or lithium selenindate (LISE). They were shown to crystallize with the β -NaFeO₂ structure (orthorhombic Pna2₁ \equiv C_{2v}⁹ symmetry, point group *mm*2), which is a distorted superstructure of the wurtzite type, as early as 1965 [8]. Hence, contrary to the other mid-IR compounds, these new materials are biaxial and isostructural to, e.g., KTiOPO₄ (KTP). The linear and nonlinear properties of LIS were briefly studied by Boyd and co-workers in the early 70's, using small and poor quality samples [9], but very few works (mainly focused on its optical bandgap characterization and photoluminescence spectra [10, 11, 12, 13, 14, 15]) have followed since until recently due to problems associated to its reliable growth in larger sizes allowing to design good optical quality single domain elements for practical applications [16]. Thin films of LiInS₂ on glass and silicon substrates were also characterized [17]. The growth problems, associated with the high chemical activity of Li, were solved recently [18] and large crystals (up to 20 mm in length) of high optical quality became available for practical nonlinear optical applications [19, 20, 21]. To our knowledge, there is only one other group which has succeeded previously in synthesizing this material with comparable size [22], but this work was also stopped recently. While only non-phase-matched second-harmonic generation (SHG) was used by Boyd and co-workers to determine the nonlinear properties of LIS [9], the first phase-matched SHG experiment using the tunable output of a pulsed LiNbO₃-OPO near 2.5 μm was reported only recently [19]. The

range of fundamental wavelengths was extended to 6 μm using the radiation from a free-electron laser and ZGP-frequency doubler [20] and rough estimation of the effective nonlinear coefficients was extracted from those measurements. Direct parametric down-conversion in the range 4.8–9 μm , using a femtosecond (200 fs) Ti:sapphire amplifier as the pump source, was simultaneously reported with an upper-bound value of the two-photon absorption (TPA) at 800 nm of $\beta=0.04 \text{ cm}^2/\text{GW}$ [21], owing to the high bandgap energy of LIS [13, 14, 22, 23]. Such a value is about 100 times less than the value for AGS or 1000 times less than for AGSe at 1.32 μm [24].

These preliminary experiments allowed to assess the potential of LIS over the existing mid-IR materials, and justify the need for a complete characterization of its optical properties. In this paper, we report new results from an intensive investigation campaign involving a network of laboratories in Europe, on the characterization of the main properties relevant for laser applications: structure and transmission (Section II), specific heat, thermal expansion and thermo-optic coefficients (Section III), accurate lattice phonon spectra (Section IV), electro-optic and piezo-electric constants (Section V), linear optical and thermo-optic dispersions (Section VI), phase-matching predictions (Section VII), nonlinear coefficients (Section VIII), parametric down-conversion (Section IX) and optical damage thresholds (Section X). The results presented here show that LIS is superior to the existing chalcopyrites in terms of high-power deep mid-IR down-conversion applications pumped directly from the near IR. The preliminary work on LISe has just started and will not be reported here [25].

II. COMPOSITION, STRUCTURE AND TRANSMISSION

Single-domain crystals of LIS are grown by the Bridgman-Stockbarger technique in a vertical setup with counter-pressure on seeds along (001) and (010) directions [8, 9, 10, 18, 26, 27, 28]. The directed crystallization is performed from a melt of elemental Li, In and S. In the melt zone the temperature is maintained at $\sim 1100 \text{ K}$ and decreases to $\sim 900 \text{ K}$ in the growth zone. The charged ampoules are moved in an optimal thermal gradient of 10–15 K/cm at a rate of $\sim 10 \text{ mm/day}$. This technique allows the growth of crystal ingots with diameters up to 20 mm and lengths up to 50 mm [18]. Although sometimes colorless to a great extent, the as-grown ingots are usually milky because of small inclusions of various phases and it is necessary to anneal them in Li₂S or S₂ vapor at temperature close to the melting point ($T_{\text{melt}} \sim 1000^\circ\text{C}$) [18]. The crystal coloration after the thermal post-growth treatment changes then from almost colorless (or slightly yellow) for as-grown, to salmon-rose tinge depending on the growth and post-growth treatment conditions and chemical composition. Optical elements with aperture up to 1 cm² and length up to 15 mm

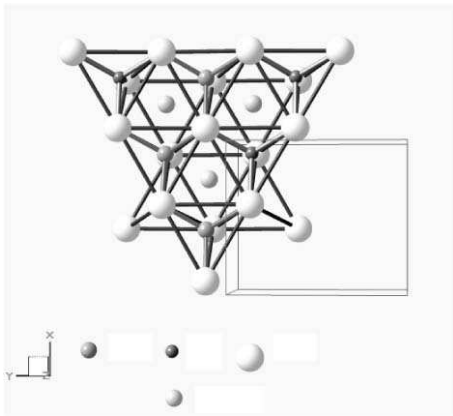


FIG. 1: Fragment of the orthorhombic unit cell structure (the box frame gives the orientation of the unit cell). The 3 empty areas materialized with light grey spheres indicate the location of octapores.

could be prepared for optical measurements or for non-linear frequency conversion.

Precise chemical analysis - using differential dissolution techniques (DDT) and inductively-coupled plasma (ICP) method - showed that the composition of colorless (or yellow tinge) and rose samples is $\text{Li}_{0.98}\text{In}_{1.03}\text{S}_{2.00}$ ($\text{Li}_{0.96}\text{In}_{1.06}\text{S}_{1.98}$) and $\text{Li}_{0.86}\text{In}_{1.04}\text{S}_{1.98}$ respectively [18]. Lithium deficit ($N_{\text{Li}} : N_{\text{In}} < 1$) is observed for all samples, the annealed rose ones being characterized by a higher sulfur content ($N_{\text{Li+In}} : N_{\text{S}} < 1$). The band-structure nature of LIS has been confirmed to be of the *direct* type (direct transitions between parabolic bands) [13, 14]. The forbidden band gap values estimated by us ($E_g = 3.72$ and 3.57 eV at 80K and 300K, respectively, which are in good agreement with previous measurements [13, 14, 22, 23]), the position of the long-wave edge of transparency ($13\mu\text{m}$ at an absorption of 6 cm^{-1}) and the crystal symmetry group were found identical for all crystal colorations although small variations in lattice parameters due to point defects were also observed [29, 30].

A detailed and general structural analysis of $\text{A}^{\text{I}}\text{B}^{\text{III}}\text{C}_2^{\text{VI}}$ compounds, where A^{I} is an alkali metal such as Li, has been given by Kish *et al* [31]. A fragment of the structure of LIS is shown in Fig. 1 (see Figs. 2.1.1-2.1.2 in Ref. [28] for the full unit cell representation). It is formed by LiS_4 and InS_4 tetrahedrons and the S^{2-} ions are arranged in hexagonal packing with tetragonal and octahedral cavities (tetra- and octapores) [31]. Compared to the denser chalcopyrite structure of AGS or AGSe [32], the β - NaFeO_2 structure of Li-chalcogenides allows the presence of empty cavities within the unit cell volume. The less dense β - NaFeO_2 structure allows in particular doping with rare-earth (RE) active ions which can be hosted inside the octapores. Such a preliminary doping experiment with Nd^{3+} ions was previously reported with the aim of investigating RE:LIS potential as a self down-converting material [33]. The values of

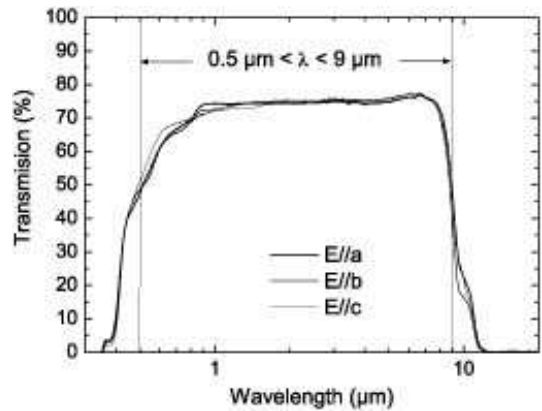


FIG. 2: Polarized transmission spectra of an annealed LIS sample (thickness 5 mm), not corrected for the Fresnel loss.

the orthorhombic lattice parameters are $a = 6.874(1)\text{\AA}$, $b = 8.033(2)\text{\AA}$, $c = 6.462(1)\text{\AA}$ for as-grown colorless LIS, and $a = 6.890(1)\text{\AA}$, $b = 8.053(1)\text{\AA}$, $c = 6.478(1)\text{\AA}$ for slightly yellowish samples. They are slightly lower than the values reported by Hoppe [8] and Boyd *et al* [9] or Kamijoh *et al* [10, 11] and Kish *et al* [34], but most closely to the last one. They modify to $a = 6.896(1)\text{\AA}$, $b = 8.058(2)\text{\AA}$, $c = 6.484(4)\text{\AA}$ for rose annealed samples. Concomitantly, the density changes from $\rho = 3.52\text{g/cm}^3$ to $\rho = 3.44\text{g/cm}^3$. We have chosen $c < a < b$ where c is the polar two-fold axis which coincides with the selection of Boyd *et al* [9]. This convention satisfies the recommendation of Roberts [35] for unique designation of the orthorhombic class $mm2$. Note that in the following, in contrast to Roberts [35] and the ANSI/IEEE Standard [36], we do not introduce an additional frame for reporting the nonlinear tensor properties but for simplification and in accordance with the tradition use the crystallographic abc frame for reporting the nonlinear optical susceptibility (see Section VII). Also, instead of small case letters xyz , as suggested by Roberts [35], we use the capital letters XYZ for designation of the principal optical axes such that $n_X < n_Y < n_Z$. Since for LIS one has $n_b < n_a < n_c$ the principal frame assignment will be $X \leftrightarrow b$, $Y \leftrightarrow a$ and $Z \leftrightarrow c$.

Fig. 2 shows the polarized transmission spectra of a thick ($L = 5\text{ mm}$) annealed optical element. Depending on the growth and annealing conditions, some absorption bands due to the various point defects - in particular excess sulfur ions occupying interstitial sites - may limit the transmission window in the visible side. These visible bands, responsible for the rose coloration of the annealed samples, restrict the range of high-transmission ($T \sim 70\%$) to $0.8 - 8.1\mu\text{m}$. The post-growth thermal treatment, however, improves considerably the transparency within the above window. The absorption coefficient $\alpha(\lambda)$ within the full transparency window deduced from the spectra amounts to $0.1 - 0.15\text{ cm}^{-1}$. These values are overestimated, since from direct laser line transmission experiments using various laser sources

in the range $0.78 - 2.53 \mu\text{m}$ and several samples the average residual absorption of a typical annealed sample was found to be lower. At $2.53 \mu\text{m}$, e.g., the total loss coefficient (absorption and scattering) estimated amounts to 0.05 cm^{-1} . At 780 nm the loss coefficient measured with a diode laser source ranged between 0.05 and 0.2 cm^{-1} depending on the strength of the weak point-defects related bands [18] seen also in Fig. 2.

III. THERMAL AND THERMO-OPTIC PROPERTIES

The thermally-related properties of a new nonlinear material are crucial in assessing its potential in real nonlinear conversion devices pumped by high power cw or pulsed lasers. The performance of devices based on mid-IR chalcogenides is often limited by deleterious thermal effects (lensing, expansion) [4, 7, 24]. The thermal figure of merit of a material can be defined by the quantity $\eta = (dn/dT)/K$ where dn/dT is the thermo-optic index variation and K is the thermal conductivity. The larger this quantity the more severe are the thermal limitations. A second thermal quantity, $\tau_D = w_0 C_p / 4K$ where C_p is the mass specific heat of the material and w_0 is the beam radius, gives the characteristic time of heat diffusion outside the pumped volume. The larger this diffusion time, the stronger the thermal lensing effects [7]. It is hence important to know C_p , K and dn/dT . In addition, the thermo-optic coefficients are needed to predict phase-matching performance in $\chi^{(2)}$ interactions. Let us point out that no data has been published on the thermal properties of single domain crystalline LIS.

A. Specific heat at constant pressure

Using Al_2O_3 as a reference we estimated $C_p(T = 300\text{K}) = 92.9 \pm 1.1 \text{ J/mol/K}$ for crystalline rose colour LIS (57.91 mg) which is only slightly higher than what has been previously measured for polycrystalline LIS (90 J/mol/K) in Ref. [37]. The temperature dependence in the $[-160^\circ\text{C}; 210^\circ\text{C}]$ range could be fitted by

$$C_p(T) = 114.02 - 5708 \times T^{-1} - 187540 \times T^{-2} \quad (1)$$

where T is in Kelvin. The general theoretical expression of $C_p(T)$ for anharmonic solids is

$$C_p(T) = 12R \left[F(x_D) + \sum_{k=1}^N c_k T^k \right] \quad (2)$$

where R is the molar gas constant, $x_D = T_D/T$ (T_D is the Debye temperature) and $F(x_D)$ is the Debye function describing the temperature dependence in the harmonic lattice vibration approximation,

$$F(x_D) = \frac{3}{x_D^3} \int_0^{x_D} \frac{x^4 e^x dx}{(e^x - 1)^2}. \quad (3)$$

The value of N and the absolute magnitudes of the coefficients c_k in the sum expansion in (2) can be considered as a measure of the degree of lattice anharmonicity, while the sign of c_k is essentially determined by the shape of the interatomic potential. In Eq. (2), the leading coefficients c_1 and c_3 were found negative for all $\text{A}^{\text{I}}\text{B}^{\text{III}}\text{C}_2^{\text{VI}}$ chalcogenide compounds, and the magnitude of c_k was found ~ 10 times higher and independent of the anion C^{2-} for Li-compounds. This means that the anharmonic contribution of the lattice potential energy is much stronger in $\text{LiInC}_2^{\text{VI}}$ compounds ($N = 4$ in Eq. 2) than in $\text{A}^{\text{I}}\text{B}^{\text{III}}\text{C}_2^{\text{VI}}$ chalcopyrite compounds ($N = 3$). In LIS, this is related to the specific nature of the Li-S bond, which is about twice weaker than the In-S bond [38]. As a consequence, the temperature dependence of $C_p(\text{LIS})$ is much weaker than for AgInS_2 and AGSe [39], and the resulting $C_p(T)$ values for LIS are the lowest of all chalcogenides. By a calorimetric absorptance (A) measurement the absorption coefficient α can be estimated from $A = mC_p\Delta T/P\Delta t = 1 - \exp(-\alpha L)$ where m is the mass in mol, ΔT is the temperature rise, P is the laser power and Δt is the irradiation time. We irradiated at 1064 nm an annealed LIS sample of dimension $5 \times 5 \times 5 \text{ mm}^3$ cut at 28° from the c crystallographic axis for light propagation in the a-c plane (mass $m = 0.438 \text{ g} = 2.356 \times 10^{-3} \text{ mol}$) and obtained an absorption coefficient of $\alpha = 0.037 \text{ cm}^{-1}$ (compare Section II).

B. Thermal expansion

The principal thermal expansion and thermo-optic coefficients were determined by using the absolute interferometric dilatometer and the experimental procedure described in Ref. [40]. A two-beam modified Mach-Zehnder interferometer arrangement is employed for dilatation measurements, while thermo-optic coefficients are obtained using the same set-up by recording changes in optical thickness of a sample acting as a thermal scanning Fabry-Perot interferometer, with the natural reflectivity of the two opposite parallel facets. Three parallelepipedic samples of dimension $5 \times 5 \times 8 \text{ mm}^3$ cut along the crystallographic axes a , b and c ($L = 8 \text{ mm}$) were used for these measurements. The samples were subjected to linear temperature ramps of $0.2^\circ\text{C}/\text{min}$ in the range $-20^\circ\text{C} - +100^\circ\text{C}$.

In a given temperature interval dT the linear thermal expansion coefficients are defined as

$$\alpha_i = \frac{1}{L_i} \frac{dL_i}{dT} \quad (4)$$

where L_i is the sample length along the direction i , with $i = a, b, c$. To be consistent with our assignment of the principal optical axes X, Y, Z in Section VI, we shall once and for all make the substitutions $X \equiv b, Y \equiv a, Z \equiv c$ in the following.

For the measurement of the thermal expansion the light source of the absolute interferometric dilatometer

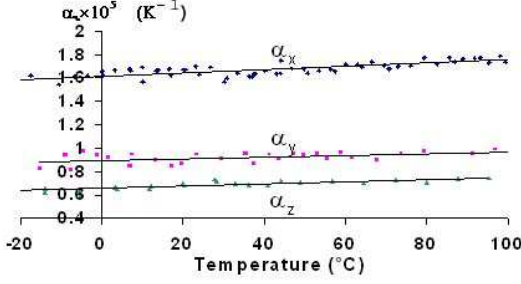


FIG. 3: Thermal expansion coefficients of LIS along the axes $X \equiv b, Y \equiv a, Z \equiv c$ from -20°C to $+100^\circ\text{C}$.

was a frequency stabilized 2-mW He-Ne laser. A plot of the experimental data is reported in Fig. 3. A linear fit of the data gives the following temperature dependence of the linear thermal expansion coefficients,

$$\alpha_X = 1.61 \times 10^{-5} + 1.4 \times 10^{-8}T, \quad (5)$$

$$\alpha_Y = 0.89 \times 10^{-5} + 0.7 \times 10^{-8}T, \quad (6)$$

$$\alpha_Z = 0.66 \times 10^{-5} + 0.9 \times 10^{-8}T, \quad (7)$$

where T is the temperature ($^\circ\text{C}$). The deviation of experimental values from these fits are less than 10^{-6} K^{-1} . At $T = 20^\circ\text{C}$ we have $\alpha_X = 1.64 \times 10^{-5} \text{ K}^{-1}$, $\alpha_Y = 0.90 \times 10^{-5} \text{ K}^{-1}$ and $\alpha_Z = 0.68 \times 10^{-5} \text{ K}^{-1}$, respectively. Such values are of the same order of magnitude (or even less) than those for AGS ($\alpha_{\parallel c} = 1.25 \times 10^{-5} \text{ K}^{-1}$, $\alpha_{\perp c} = -1.32 \times 10^{-5} \text{ K}^{-1}$) [41] and AGSe ($\alpha_{\parallel c} = 1.68 \times 10^{-5} \text{ K}^{-1}$, $\alpha_{\perp c} = -0.78 \times 10^{-5} \text{ K}^{-1}$) [42].

However, the main difference with those chalcopyrites is that LIS does not display their anomalous thermal expansion behaviour (opposite sign of α along the two orthogonal directions) that is a major source of thermo-mechanical stress in high power applications [32]. In contrast, LIS expands in the same direction as temperature increases and exhibits a rather weak temperature dependence. This favorable situation is related to the specific nature of the weak Li-S bond already evoked in the previous subsection.

C. Thermo-optic coefficients

We shall again make use of the labels $X \equiv b, Y \equiv a, Z \equiv c$ denoting the principal optical axes to describe the change of the index of refraction versus temperature, for a light polarized along one of these principal axes and propagating along another principal direction. For a light wave polarized along direction p_j and propagating along direction e_i , we define the coefficient γ_{ji} related to thermal changes in optical thickness (path) by

$$\gamma_{ji} = \frac{1}{n_j L_i} \frac{d(n_j L_i)}{dT} \quad (8)$$

where n_j and L_i are respectively the refractive index and the length of the sample, with $i, j = X, Y$ or Z and $i \neq j$.

TABLE I: Principal normalized thermo-optic coefficients $\beta_j = \frac{1}{n_j} \frac{dn_j}{dT} = a_1 + a_2 T$ of LIS [Eq. (10)] at four laser wavelengths.

λ (μm)	β_j ($^\circ\text{C}^{-1}$)	$10^5 a_1$ ($^\circ\text{C}^{-1}$)	$10^8 a_2$ ($^\circ\text{C}^{-2}$)
0.4765	β_X	3.41 ± 0.06	3.1 ± 0.3
	β_Y	4.11 ± 0.07	4.6 ± 0.9
	β_Z	4.08 ± 0.02	4.7 ± 0.4
0.6328	β_X	2.28 ± 0.07	1.5 ± 0.4
	β_Y	2.76 ± 0.05	2.1 ± 0.4
	β_Z	2.69 ± 0.01	2.4 ± 0.1
1.0642	β_X	1.75 ± 0.07	1.0 ± 0.06
	β_Y	2.10 ± 0.11	1.3 ± 0.5
	β_Z	2.03 ± 0.08	1.3 ± 0.1
3.392	β_X	1.50 ± 0.07	0.7 ± 0.17
	β_Y	1.83 ± 0.14	1.1 ± 0.5
	β_Z	1.73 ± 0.03	1.0 ± 0.02

The normalized thermo-optic coefficients $\beta_j = \frac{1}{n_j} \frac{dn_j}{dT}$ are derived from (4) and (8) and given by

$$\beta_j = \gamma_{ji} - \alpha_i. \quad (9)$$

As evident from Eq.(9), the knowledge on the values of the thermal expansion is prerequisite for the interferometric determination of the thermo-optic coefficients at a given wavelength. For the orthorhombic symmetry of LIS it can be seen that each β_j may be obtained for two directions of light propagation. This has been performed at four laser wavelengths, and the resulting linear fits to

$$\beta_j(\lambda, T) = a_1(\lambda) + a_2(\lambda)T \quad (10)$$

where T is measured in $^\circ\text{C}$ are summarized in Table I. The indicated uncertainties in the parameters a_1 and a_2 represent the deviation from the mean value determined from the two possible propagation directions e_i for a given orientation p_j of light polarization. At $\lambda = 1064 \text{ nm}$ and $T = 20^\circ\text{C}$, one has $dn_X/dT = 3.725 \times 10^{-5} \text{ K}^{-1}$, $dn_Y/dT = 4.545 \times 10^{-5} \text{ K}^{-1}$, $dn_Z/dT = 4.467 \times 10^{-5} \text{ K}^{-1}$. Compared with the thermo-optic coefficients of AGS [43], these values are about 5 times lower. Dispersion relations based on those wavelength-dependent data will be derived in Subsection VIB.

IV. VIBRATIONAL PROPERTIES

The vibrational properties have been investigated by means of Raman spectroscopy and infrared reflectivity in polarized light at room temperature. The group theory analysis shows that, at the zone centre for the β -NaFeO₂ structure, the 48 normal phonon modes are distributed among the various irreducible representations of the C_{2v}^9 factor group as follows:

$$\Gamma^{vib} = 12A_1 + 12A_2 + 12B_1 + 12B_2. \quad (11)$$

The three acoustic phonon modes have A_1 , B_1 and B_2 symmetries; the 45 remaining (optical) modes are

Raman-active. A_1 modes will be active when the experimental configuration selects a diagonal aa , bb or cc component of the Raman tensor, while the selection of ba , ca and cb components will respectively allow the observation of the optical phonons of A_2 , B_1 and B_2 symmetry. A_2 -type phonons being infrared inactive, the IR-reflectivity spectra should then contain 11 polar modes of each A_1 , B_1 and B_2 symmetries, with dipole moment respectively parallel to c , a and b crystallographic axes. In theory, every optical phonon may then be observed by means of IR-reflectivity and/or Raman-scattering. Nonetheless, depending on various factors such as the more or less polar character of bonds, even an active mode may be unobservable.

To obtain results on every phonon type, we used two LIS rose-tinge samples cut from the same ingot, with sizes $4 \times 4 \times 5 \text{ mm}^3$ and parallel optically polished facets ($4 \times 4 \text{ mm}^2$) normal to a and c axes. Infrared reflection spectra were recorded in the spectral range $18.3 - 600 \text{ cm}^{-1}$, and this whole range of data was used to adjust the parameters of the dielectric permittivity model shown in Eq.(12). The experimental spectra, recorded at quasi-normal incidence (at an angle of incidence of 6°) with an electric field polarization parallel to a , b and c axes, are shown in Fig. 4 (symbols). As can be seen from these graphs, each reflectivity spectrum is rather complex and exhibits several more or less overlapping bands, and the high-energy band(s) in each polarization generally show some additional structure (slight inflexion in the band shape) that suggests, in addition to a strong mode, the presence of several other modes contributing to the same band. Actually, from the numerical analysis of the experimental results, it is found that for each direction of polarization, there are three polar modes in the high frequency band ($350 - 420 \text{ cm}^{-1}$) and medium frequency band ($250 - 350 \text{ cm}^{-1}$) and the remaining five polar modes, not all observable in Fig. 4, are in the low frequency region ($< 250 \text{ cm}^{-1}$).

Polarized micro-Raman spectra were recorded using a Raman spectrometer equipped with a confocal microscope and a liquid- N_2 cooled CCD detector in the region $12 - 600 \text{ cm}^{-1}$ in triple subtractive configuration with an 1800 gr/mm grating. To increase the quality and resolution of the spectra, we chose to use the 647 nm red line of an argon-krypton laser ($P=100 \text{ mW}$) which experiences lower absorption loss than a green laser [44]). To avoid possible influence of surface defects, the confocal microscope focused the laser beam at a depth of $60 \mu\text{m}$ under the surface. A scattering geometry will be described by the notation $e_1(p_1p_2)e_2$ [45] where e_i identifies the propagation direction of the laser light, polarized along p_i , e and p being a , b or c crystallographic axes; the subscripts $i = 1$ and 2 refer to incident and scattered beams respectively. Fig. 5 shows some of the experimental spectra. The Raman spectra are dominated by a strong mode of A_1 symmetry at $\sim 268 \text{ cm}^{-1}$, also apparent in the IR reflectivity spectra for $E//b$ and $E//c$.

Due to the respective mass of the atoms, high (low) fre-

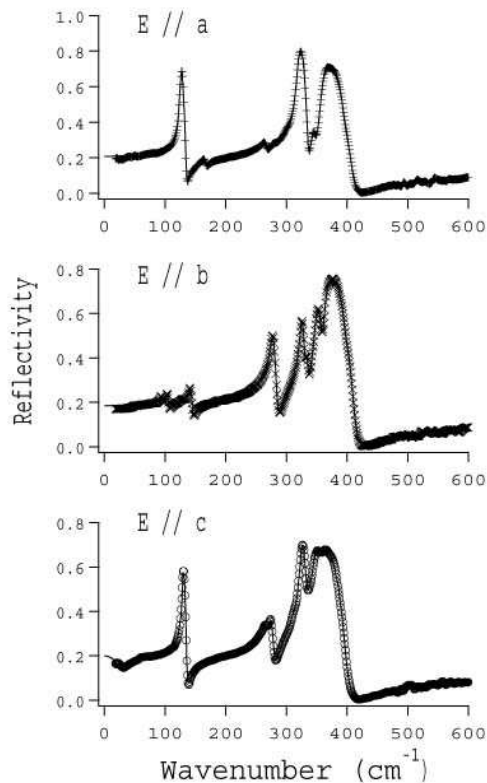


FIG. 4: Infrared reflection curves (symbols) recorded with polarized light with an electric field parallel to the crystallographic axes a - B_1 modes -, b - B_2 modes - and c - A_1 modes. The continuous lines represent in each case the best-fit reflectivity curves calculated with the model in Eqs.(12)-(13).

quency modes obviously imply movements of Li-S (In-S) bonds. Phonons of medium frequency ($250 - 350 \text{ cm}^{-1}$), visible in both IR-reflectivity and Raman scattering, are attributed to In-S bonds [23] while those of highest frequency (above 350 cm^{-1} , Fig. 4) that give rise to strong IR bands but no observable Raman line are due to weaker Li-S bonds [38]. Polar modes TO \approx LO splitting observed in the infrared measurements for any of the explored polarizations is rather important in the high frequency region (strong IR-bands) which attests for a high polar (ionicity) character of Li-S bonds in this crystal. The splitting decreases with the phonon frequency to become so small for low frequency modes that no corresponding band appears in the reflectivity spectrum which indicates a mostly covalent character of the In-S bonds. However, even if a phonon cannot be observed by means of IR-reflectivity, its Raman activity may be high, which is the case for modes lying below 100 cm^{-1} . Actually intense Raman lines appear in the low and mid-frequency region, when almost no line can be detected above roughly 350 cm^{-1} . In order to fit the experimental IR-reflectivity spectra, and get the best-fit reflectivity curves (lines in Figure 4, in a good agreement with experimental points) we used the so-called *four-parameter model*, convenient

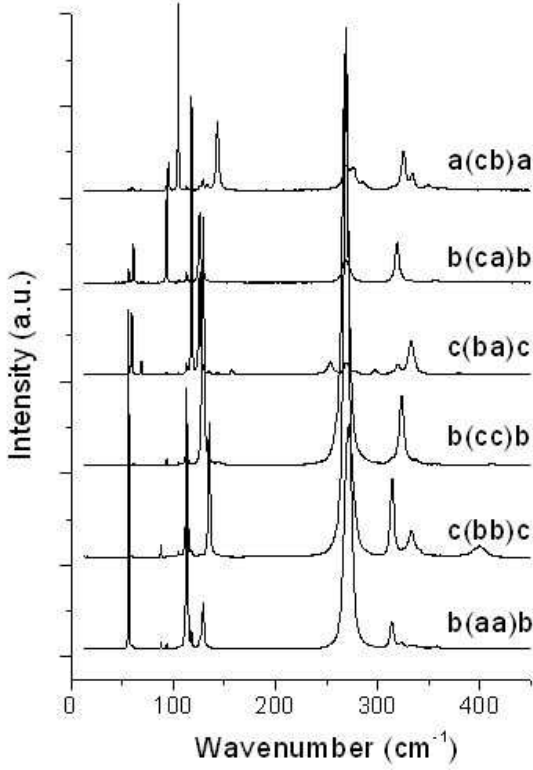


FIG. 5: Polarized Raman spectra (shifted for reasons of clarity) recorded at room temperature. The experimental configurations $b(aa)b$, $c(bb)c$, $b(cc)b$ correspond to A_1 modes, $c(ba)c$ to A_2 modes, $b(ca)b$ to B_1 modes and $a(cb)a$ to B_2 modes.

to represent even asymmetrical and wide bands [46]. This model expands the factorized form of the dielectric permittivity function as

$$\varepsilon(\omega) = \epsilon' - i\epsilon'' = \varepsilon_\infty \prod_{j=1}^N \frac{\Omega_{j,LO}^2 - \omega^2 + i\gamma_{j,LO}\omega}{\Omega_{j,TO}^2 - \omega^2 + i\gamma_{j,TO}\omega} \quad (12)$$

to fit a reflectivity curve described by the Fresnel formula

$$R(\omega) = \left| \frac{\sqrt{\varepsilon(\omega)} - 1}{\sqrt{\varepsilon(\omega)} + 1} \right|^2. \quad (13)$$

In the β -NaFeO₂ structure, the model implies for a given polarization N damped oscillators, the number N being at most equal to 11 (number of theoretically observable modes, predicted in this structure by group theory analysis). The j -th damped oscillator represents the j -th observed infrared active couple of modes, characterized by four adjustable parameters, namely the longitudinal $\Omega_{j,LO}$ and transverse $\Omega_{j,TO}$ angular frequencies, and the corresponding damping frequencies $\gamma_{j,LO}$ and $\gamma_{j,TO}$. The high-frequency limit values of the dielectric constant is also adjusted to yield $\varepsilon_\infty(A_1)=3.99$, $\varepsilon_\infty(B_1)=4.09$, $\varepsilon_\infty(B_2)=3.97$.

Table II lists the wavenumbers $\bar{\nu}_j = \Omega_j/2\pi c$ and damping rates $\bar{\gamma}_j = \gamma_j/2\pi c$ (expressed in cm^{-1}) of the observed

optical phonons deduced from IR-reflectivity and/or Raman scattering experiments, assigned to the various irreducible representations of the C_{2v}^9 factor group. These data allow to compute the linear dielectric properties of LIS in the far-IR range, using Eq.(12). Typically, TO and LO frequencies deduced from IR-reflectivity experiments are determined to better than 1 cm^{-1} . The precision of a Raman-active phonon frequency is also generally better than 1 cm^{-1} , except for broad and low-intensity lines for which it decreases to 2 cm^{-1} . The transverse or longitudinal character of the Raman-active modes for A_1 , B_1 and B_2 symmetries has been determined with the help of the IR reflectivity results where this TO or LO character is immediate. Non-observed IR-active modes indicate a small $\text{TO} \approx \text{LO}$ splitting and generally did not allow an accurate determination of TO and LO frequencies from Raman spectra, but only of a mean value labelled by $\text{TO} \approx \text{LO}$. A few Raman lines have been attributed to an interference by an intense line active in another geometry. These Raman results complement those from previous studies performed with unpolarized [23, 26, 28] and polarized light [47].

The accurate determination of the frequencies in Table II allows to estimate the interatomic bonding force constants in LIS, using the theoretical considerations developed by Neumann about the correlation between the vibrational modes of compounds with sphalerite, chalcopyrite and β -NaFeO₂ structures [48]. According to this model the vibrational spectrum of a crystal with β -NaFeO₂ structure contains two sphalerite-like modes the TO-frequencies of which are nearly independent of the polarization direction. Further, one of these sphalerite-like modes always corresponds to the highest $\bar{\nu}_{\text{TO}}$ frequency found in the IR reflectivity spectra. If the interaction between the atoms is restricted to next-nearest neighbors which is justified by the high bond ionicities in Li-containing ternary compounds, the wavenumbers of the transverse optical modes of these sphalerite-like modes in $\text{LiB}^{\text{III}}\text{C}_2^{\text{VI}}$ are given by [49]

$$\bar{\nu}_{\text{TO},k}^2 = \frac{1}{\pi^2 c^2} (\alpha_k - \delta\alpha_k) \left(\frac{1}{m_k} + \frac{1}{m_C} \right) \quad (14)$$

with the superscript k = in the first parenthesis denoting Li-C or B-C cation-anion bonds (in the present case, $C = \text{S}$ and $B = \text{In}$). Here c is the speed of light, α_k the mechanical bond-stretching force constant, m_k the mass of the cation and m_C the mass on the chalcogen anion ($C = \text{S}^{2-}$). The quantity $\delta\alpha_k$ accounts for the fact that in the case of IR active modes the local atomic displacements give rise to a non-vanishing net dipole moment per unit cell and thus, to additional dipole-dipole interactions. It is given by $\delta\alpha_k = \sqrt{3}(e_k)^2/(16\varepsilon_0 s_k^3)$, where s_k is the average bond length ($s_{\text{Li-S}} = 0.2438 \text{ nm}$, $s_{\text{In-S}} = 0.2452 \text{ nm}$), $e_k = 0.28ef_k(Z_k + Z_C)$ is an effective charge depending on the bond ionicity f_k and the valences of the cation and anion participating to the bond. In Ref. [38], from an unpolarized IR reflectivity spectrum of polycrystalline LIS restricted to the re-

TABLE II: Zone-center phonon wavenumbers ($\bar{\nu}_{\text{TO}}/\bar{\nu}_{\text{LO}}$) and damping ($\bar{\gamma}_{\text{TO}}/\bar{\gamma}_{\text{LO}}$), in cm^{-1} , deduced from IR reflectivity and Raman scattering experiments at room temperature for the various symmetry-adapted polarization configurations. The transverse (TO) and/or longitudinal (LO) character of the observed Raman-active phonons have been determined with the help of the IR reflectivity results (the notation TO \approx LO means that the splitting is too weak to be unambiguously identified).

Phonon symmetry	IR reflectivity		Raman scattering
	Wavenumbers $\bar{\nu}_j$	Dampings $\bar{\gamma}_j$	
A ₁ TO/LO (cm ⁻¹)	-/-	-/-	56.4 (TO \approx LO)
	-/-	-/-	88.1 (TO \approx LO)
	-/-	-/-	112.7/113.3
	128.6/138.2	3.0/4.4	129.1/135.2
	266.0/267.1	8.5/8.7	268/269
	274.2/279.2	9.2/8.7	273/-
	274.2/279.2	9.2/8.7	273/-
	313.6/313.8	4.9/5.0	314 (TO \approx LO)
	323.7/333.7	6.2/11.3	323.4/333
	341.7/356.0	14.3/13.9	341/-
A ₂ (cm ⁻¹)	357.0/373.0	14.5/14.7	357/-
	373.1/399.0	14.3/16.5	-/399
	IR inactive		59.4
			68.7
			117.8
			125.9
			157.4
			253.5
			297.4
			319.4
			332.5
B ₁ TO/LO (cm ⁻¹)	-/-	-/-	61.1 (TO \approx LO)
	-/-	-/-	93.5 (TO \approx LO)
	125.8/133.4	2.6/3.0	125.8/133.3
	164.9/166.0	8.4/9.0	165 (TO \approx LO)
	264.9/266.3	9.3/10.3	267 (TO \approx LO)
	303.3/303.7	9.4/9.2	-/-
	318.3/334.6	5.0/7.2	318.7/-
	343.6/347.8	11.2/10.4	-/-
	356.4/375.9	10.4/22.8	356.5/-
	376.7/395.8	21.9/23.1	-/-
B ₂ TO/LO (cm ⁻¹)	400.4/408.6	29.7/12.4	-/-
	-/-	-/-	59.3 (TO \approx LO)
	96.1/96.4	3.3/3.1	96 (TO \approx LO)
	104.7/105.7	4.8/5.2	104.7/105.5
	132.0/132.5	10.2/10.1	133 (TO \approx LO)
	142.7/144.9	6.1/6.9	143.2 (TO \approx LO)
	276.5/285.1	8.0/8.4	276.2/285
	324.6/329.8	5.9/7.3	325.2 (TO \approx LO)
	333.4/336.0	7.2/7.5	334 (TO \approx LO)
	348.0/358.4	10.3/8.9	348/-
	362.2/397.7	8.6/11.0	362/-
	398.6/410.4	11.1/11.9	-/-

gion 200 - 400 cm^{-1} , the highest-frequency TO/LO mode identified corresponds to 356/406 cm^{-1} and the second TO/LO sphalerite-like mode to 323/334 cm^{-1} . Actually from the inspection of Table II, the highest-frequency sphalerite-like modes with nearly identical frequencies in B₁ and B₂ symmetries are respectively the 400.4/408.6 cm^{-1} and 398.6/410.4 cm^{-1} (this mode is not observed in A₁). The second sphalerite-like mode is recognized from Table II as the 323.7/333.7 cm^{-1} (A₁), 318.3/334.6 cm^{-1} (B₁), 324.6/329.8 cm^{-1} (B₂), close to the value identified in Ref. [38]. The Li-S bond force constant deduced from Eq.(14) by Sobotta *et al* [38], $\alpha_{\text{Li}} = 24.7 \text{ N/m}$, is then underestimated by $(400.4/356)^2 = 24\%$ while the In-S bond force constant, deduced from the second sphalerite-like mode remains unchanged to $\alpha_{\text{In}} = 53.4 \text{ N/m}$. But

even with this slight correction, the Li-S bond remains still about twice weaker than the In-S bond. In contrast the strength of the Ag-C^{VI} bond in chalcopyrite compounds is more comparable to that of the B^{III}-C^{VI} bonds [38], underlining the specific nature of the lithium-chalcogen bond in crystals with tetrahedral coordination of the atoms. As a consequence, the increased lattice phonon energy of LIS, as compared with AGS or AGSe, favors heat dissipation, hence a higher thermal conductivity is expected. Indeed, an unpublished measurement of LIS thermal conductivity yielded $K_a = 6.0 \text{ W/(m}\cdot\text{K)}$, $K_b = 6.2 \text{ W/(m}\cdot\text{K)}$ and $K_c = 7.6 \text{ W/(m}\cdot\text{K)}$ [50], i.e. 5 times larger than for AGS and of the same magnitude as for LiNbO₃.

A last important feature from the vibrational spectra is

that the phonon spectrum for LIS is located at wavenumbers below 410 cm^{-1} . The IR wavelength cut-off ($8.1 \mu\text{m}$) in Fig. 2 quite exactly corresponds to three times this highest energy phonon. The long wavelength shape of the transmission curves - and limit of the transparency range - seems then to be simply due to multiphonon processes. It is worth mentioning that, although the vibrational investigations have used rose tinge samples, the phonon spectrum should not depend on coloration since all LIS samples display the same IR cutoff edge, with or without annealing.

V. PIEZO-ELECTRIC AND ELECTRO-OPTIC COEFFICIENTS

A. Apparent electro-optic coefficients

The measurement of electro-optic coefficients involves the determination of changes in optical thickness when applying an electric field to the material. LIS belongs to the symmetry class $mm2$ for which the electro-optic tensor exhibits 5 nonzero components, namely r_{13} , r_{23} , r_{33} , r_{42} and r_{51} [36]. In this subsection we will describe the electro-optic effect in the principal optic frame where XYZ are the axes of the index ellipsoid which as we shall see in the next section coincide with the crystallographic bac axes. We will address only the r_{i3} 's coefficients that can be obtained by applying a field E_3 along the Z -axis which does not lead to a rotation of the ellipsoid. Optical interferometric methods may be advantageously used in this case for their determination. An applied electric field \mathbf{E} , with respective components (E_1, E_2, E_3) along the principal axes (X, Y, Z) , will modify the index ellipsoid according to

$$(n_X^{-2} + r_{13}E_3)X^2 + (n_Y^{-2} + r_{23}E_3)Y^2 + (n_Z^{-2} + r_{33}E_3)Z^2 + 2r_{42}E_2YZ + 2r_{51}E_1XZ = 1. \quad (15)$$

The new indices $n_i(E_3)$ ($i \equiv 1, 2, 3 \equiv X, Y, Z$) are given by

$$n_i(E_3) = n_i - \frac{1}{2}n_i^3r_{i3}E_3 \quad (16)$$

where $\delta(n_i) = -\frac{1}{2}n_i^3r_{i3}E_3$ represents the variation of the refractive index n_i .

Due to the piezo-electric effect the field E_3 will also generate a variation $\delta(L_j)$ of the crystal thickness L_j along a given direction e_j such that

$$\delta(L_j) = L_j\bar{d}_{3j}E_3 \quad (17)$$

where \bar{d}_{3j} ($j = 1, 2, 3$) are components of the piezo-electric tensor [36]. For a light wave propagating along direction e_j and polarized along direction p_i of the crystal the variation $\delta(n_iL_j)$ of the optical path n_iL_j induced by an applied electric field E_3 will be

$$\delta(n_iL_j) = n_iL_j \left(\bar{d}_{3j} - \frac{1}{2}n_i^2r_{i3} \right) E_3. \quad (18)$$

TABLE III: Apparent electro-optic coefficients of LIS; 3(X) and 3(Y) represent the values of r_{33}^{eff} obtained for a light propagation along X and along Y, respectively.

i	r_{i3}^{eff} (pm/V)
1	2.18 ± 0.04
2	2.82 ± 0.33
3(X)	0.93 ± 0.03
3(Y)	0.11 ± 0.02

We define the *effective* electro-optic coefficients as

$$r_{i3}^{\text{eff}} = -\frac{2}{n_i^2} \left(\bar{d}_{3j} - \frac{1}{2}n_i^2r_{i3} \right) \quad (19)$$

with $j = 1, 2$, which represent in fact the (apparent) electro-optic coefficients obtained in most experiments where the piezo-electric contribution is ignored. The measurements of the r_{i3}^{eff} 's were performed by using the technique of Phase-modulated Thermal Scanning Interferometry (PTSI) [51]. In this method, as for the measurements of thermo-optic coefficients, the sample acts as a Fabry-Perot thermal scanning interferometer in which phase modulation is achieved by applying an AC field E_3 along the Z axis. Various configurations of light polarization (E_X, E_Y, E_Z) and wave vector \mathbf{k} (k_X, k_Y) were used to determine the apparent electro-optic coefficients of LIS.

The two LIS samples of aperture $5 \times 5 \text{ mm}^2$ used for the thermo-optic data measurements with lengths $L = 8 \text{ mm}$ along the X and Y propagation axes were supplied with gold evaporated electrodes on their Z facets. The low frequency (480 Hz) applied voltage was 200 V peak-to-peak and linear temperature ramps of $0.2^\circ\text{C}/\text{min}$ were used from 20°C to 55°C . Measurements of apparent electro-optic coefficients were performed at $1.064 \mu\text{m}$ by using a 100mW TEM₀₀ single-frequency Nd:YAG laser. In the scanned temperature interval a constant value has been observed for each of them; they are summarized in Table III. These data feature a quite weak electro-optic effect in LIS and the large discrepancy observed between $r_{i3(X)}^{\text{eff}}$ and $r_{i3(Y)}^{\text{eff}}$ suggests a strong contribution of the piezo-electric effect to the apparent electro-optic one.

B. Piezo-electric and pure electro-optic coefficients

The non-vanishing piezo-electric coefficients \bar{d}_{31} , \bar{d}_{32} and \bar{d}_{33} were measured by using the modified Mach-Zehnder arrangement of the absolute interferometric dilatometer in a manner similar to the one employed for dilatation measurements. Phase modulation of the interference pattern is performed by applying to the samples the same voltage and same thermal scanning procedure as described previously. The algebraic sign of the coefficients was attributed according to the ANSI/IEEE Standard 176-1987 on piezo-electric crystals [36] and

we have found in pm/V units and in the XYZ frame: $\bar{d}_{31} = -5.6 \pm 0.1$, $\bar{d}_{32} = -2.7 \pm 0.2$ and $\bar{d}_{33} = +7.5 \pm 0.2$.

From Equation (19) we determine the pure electro-optic coefficients $r_{13} = 1.0$ pm/V, $r_{23} = 0.4$ pm/V and $r_{33} = -1.3$ pm/V which reveals a rather small true electro-optic effect compared to the piezo-electric one. The relative uncertainty in these values is close to 15%. These measurements confirm that, as AGS or AGSe, LIS is a poor candidate for electro-optic or piezo-electric based devices. A comparison of our results with earlier data of Negran *et al* [52] cannot be meaningful since the r_{13} , r_{23} and r_{33} that were measured there did not account for the piezo-electric contribution and were not determined independently, but as a linear combination.

C. Comparison of the electro-optic and pyroelectric coefficients

From the anharmonic oscillator model developed by Garrett [53], Soref [54] yields a semi-empirical relationship between the pyroelectric coefficient at constant stress ($p^\sigma = (\frac{\Delta P_s}{\Delta T})_\sigma$) and the second-order electronic susceptibility $\chi^{(2)}$ describing the linear (true) electro-optic effect:

$$p^\sigma = \chi^{(2)}(\omega \pm 0; \omega, 0) 2C_v \frac{\epsilon_0 m_e^2 (\omega_e^2 - \omega^2)^2}{\mu \omega_i^2 N_A e^2} \left(\frac{3A + B}{C + 3D} \right). \quad (20)$$

The pyroelectric coefficient p^σ gives the variation of the spontaneous polarization ΔP_s induced by a temperature variation ΔT . The parameters m_e and e are the mass and charge of the electron, ω_e and ω_i are respectively the electronic and ionic resonance frequencies, C_v is the molar specific heat at constant volume (which differs from the specific heat at constant pressure C_p measured in Subsection III A by a negligible quantity) and N_A the Avogadro number. The constant terms A, B, C and D are the coefficients related to the third order expansion of the crystal potential energy in the electronic and ionic coordinate system q_e and q_i [54]. The ratio $(3A + B)/(C + 3D)$ indicates the extent to which the predominant ionic contribution to the anharmonic potential at $\omega \approx \omega_i$ differs from the predominant electronic one at $\omega \gg \omega_i$. This ratio is expected to be constant whatever the material, suggesting a linear relationship between the electro-optic and pyroelectric coefficients. This hypothesis was verified for a few known materials, mostly of the oxide type [54].

By using $C_v = C_p$ and $\chi_{333}^{(2)} = n_3^4 r_{33}$ from the previous subsection, the pyroelectric coefficient measured previously [55] as a function of temperature and its value extrapolated at 300 K, $p^\sigma = 6 \times 10^{-10}$ C · cm⁻² K⁻¹, we observe that Soref's hypothesis is confirmed for the ternary semiconductor LIS, as it was already shown for the binary one CdS [54]. We note also that a rather good estimate of the pyroelectric effect may be deduced from electro-optic measurements and vice versa, but this

requires at first an accurate determination of the piezo-electric contribution.

VI. LINEAR OPTICAL AND THERMO-OPTIC DISPERSIONS

We now address, in light of the vibrational spectra results, the most important data for a nonlinear material: linear optical and thermo-optic dispersion relations that allow to predict accurately the phase-matching directions and temperature tunability.

A. Sellmeier equations at room-temperature

The only available dispersion data of LIS, measured using the minimum deviation technique, were compiled by Boyd *et al* in 1973 [9] and fitted to one-pole (UV) Sellmeier equations [56] reproduced also in Refs. [21, 57, 58]. Although the accuracy of their index determination was not reported, from subsequent nonlinear phase-matched conversion experiments it appeared that the Sellmeier equations based on their data are accurate to predict the birefringence (via angle acceptance bandwidth measurements [19]), but fail to predict accurately the absolute phase-matching directions. Discrepancies of several degrees from the expected phase-matching angles were reported [20]. Such deviations cannot be attributed to the X-ray sample orientation uncertainties ($\pm 0.5^\circ$). Furthermore, we have checked that the phase-matching angles, and hence the linear refractive indices, are independent of crystal coloration or exact stoichiometry.

Following the standard convention for assigning the principal axes (X, Y, Z) to the crystallographic axes (a, b, c), e.g. $n_X < n_Y < n_Z$, one has $X \leftrightarrow b$, $Y \leftrightarrow a$ and $Z \leftrightarrow c$ for LIS since $n_b < n_a < n_c$. A phase-matching direction will be labelled by (θ, φ) , where θ is the angle of the wavevector respective to the polar Z axis and φ is the azimuthal angle between its projection in the $X-Y$ plane and the X axis. To refit the Sellmeier equations given in Ref. [56], we have used the experimental type-II (eoe, oeo) SHG angles measured in the fundamental wavelength range $\lambda \in [2.5 - 6] \mu\text{m}$ [20, 44], supplemented with new recent data derived from type-II (eoe) difference-frequency generation (DFG) in the X-Y plane (see subsection IX B), where in the wavelength-tuning mode, mid-IR down-conversion in the range $\lambda_1 \in [6.6 - 7] \mu\text{m}$ was achieved at normal incidence. Table IV compiles the experimental phase-matching data used to derive the following room-temperature ($T = 20^\circ\text{C}$) two-pole Sellmeier equations, valid over the full transparency window, using

a nonlinear least-square fit of the data,

$$n_X^2 = 6.686059 + \frac{0.1385833}{\lambda^2 - 0.05910334} + \frac{2047.46509}{\lambda^2 - 897.7476} \quad (21)$$

$$n_Y^2 = 7.095493 + \frac{0.1422326}{\lambda^2 - 0.06614640} + \frac{2511.08936}{\lambda^2 - 988.2024} \quad (22)$$

$$n_Z^2 = 7.256327 + \frac{0.15072}{\lambda^2 - 0.06823652} + \frac{2626.10840}{\lambda^2 - 983.0503} \quad (23)$$

In Eqs.(21)-(23), the wavelengths are expressed in microns. The three IR wavelength poles $\lambda_{IR}(X) = 29.96 \mu\text{m}$, $\lambda_{IR}(Y) = 31.44 \mu\text{m}$, $\lambda_{IR}(Z) = 31.35 \mu\text{m}$ (i.e. $\bar{\nu}(X) = 333.7 \text{ cm}^{-1}$, $\bar{\nu}(Y) = 318.1 \text{ cm}^{-1}$, $\bar{\nu}(Z) = 318.9 \text{ cm}^{-1}$) correspond to the medium-frequency phonon band-centers of symmetry B_2 , B_1 and A_1 respectively, attributed to the In-S vibrations (see Table II). We note that another two-pole Sellmeier set of equations that recently appeared [59] is based on the old index data of Boyd et al. [9] while the mid-IR poles were not associated with phonon frequencies. Fig. 6 displays the principal indices of refraction deduced from Eqs.(21)-(23). No index crossing ($n_o(\lambda) = n_e(\lambda)$) is found in the blue part of the dispersion data, in contrast with the uniaxial AGS [43]. The two optic axes, lying in the X-Z plane, determine the propagation directions where the index of refraction is independent of the polarization. The angle between the two optic axes is $2V_Z$ where V_Z is the angle of each axis with the polar Z-axis. V_Z is wavelength-dependent and can be calculated from [3]

$$\sin V_Z = \frac{n_Z(n_Y^2 - n_X^2)^{1/2}}{n_Y(n_Z^2 - n_X^2)^{1/2}}. \quad (24)$$

Fig. 7 plots V_Z as a function of the wavelength, using Eqs.(21)-(23) (solid line) and using the Sellmeier equations of Ref. [56] (dashed line). Let us note the different behavior for $\lambda < 1 \mu\text{m}$ (absence of a retracing behavior). Note that although the principal indices on which the

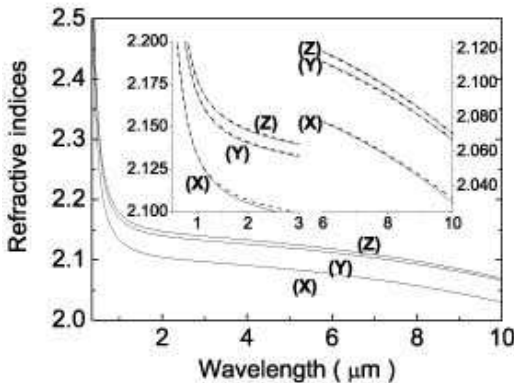


FIG. 6: Principal refractive indices of LiInS_2 as computed from Eqs.(21)-(23). The inset plots show the UV and mid-IR portions on an expanded scale and also a comparison with a calculation based on the Sellmeier expansions from Ref. [56] (dashed lines).

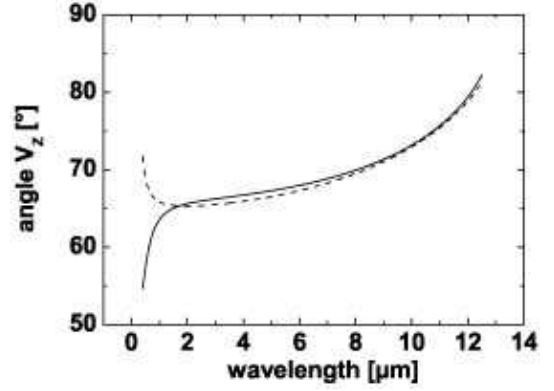


FIG. 7: Angle V_Z between the optic axes and the Z-axis in LIS calculated with the Sellmeier expansion of Ref. [56] (dashed line), and the new Sellmeier expansion (Eqs.(21)-(23)) (solid line).

old dispersion relations are based were measured from the minimum deviation technique in 1973 [9], the absorption coefficient of the prism samples used then was quite different (much larger than in Fig. 2 up to about $2.5 \mu\text{m}$) which obviously is the reason for the difference observed in Fig. 7. Since $V_Z > 45^\circ$ LIS is a negative biaxial crystal. At longer wavelengths it can be regarded as quasi-uniaxial, which is a consequence of the fact that the two indices n_Y and n_Z are very close. Therefore no phase-matching can be expected for propagation directions in the vicinity of the X-principal axis.

The agreement between the experimental phase-matching data used to derive Eqs.(21)-(23) and the calculated ones is illustrated in Fig.8 (solid lines) and Table IV. The accuracy of phase-matching angle prediction is $\pm 1.5^\circ$. The eight last SHG points in Fig. 8 were discarded from the nonlinear fit for obvious lack of reliability. Only a two-pole form leads to the smallest residual discrepancies between calculated and experimental data, while the former one-pole Sellmeier equations [56] are unable to predict SHG near the cut-off wavelength of $\sim 6 \mu\text{m}$. Let us note that there is a discrepancy of $\sim +6^\circ$ between the experimental phase-matching angles for SHG in the Y-Z plane and the ones calculated with the old Sellmeier equation, which means that the Y-Z birefringence given by Eqs. (21)-(23) is more accurate. The previous one-pole Sellmeier equations also predict DFG wavelengths $\sim +40 \text{ nm}$ longer than experimentally observed. Under the usual designation $\lambda_1 \geq \lambda_2 > \lambda_3$ the FWHM DFG angular acceptance (FWHM) measured at fixed wavelengths was $\Delta\varphi = 0.19^\circ$ for a crystal length of 10 mm, i.e. much smaller than the uncertainty on crystal orientation ($\pm 0.5^\circ$). Hence the uncertainty ($\pm 1 \text{ nm}$ at maximum) of wavelength measurement in Table IV cannot explain the $\sim 40 \text{ nm}$ shift observed with the previous Sellmeier equations, confirming the increased accuracy in dispersion provided by Eqs.(21)-(23).

TABLE IV: Phase-matching conditions for type-II SHG and DFG in LiInS₂.

	Wavelength (nm) ^a			Phase-Matching Angles (θ, φ) ^b	
	λ_1	λ_2	λ_3	Measured	Calculated
SHG (XY: <i>eoe</i>)	2366	2366	1183	(90, 82.1)	(90, 83.908)
	2469	2469	1234.5	(90, 73.1)	(90, 72.755)
	2527	2527	1263.5	(90, 69.8)	(90, 69.235)
	2583	2583	1291.5	(90, 67.4)	(90, 66.507)
	2900	2900	1450	(90, 57.9)	(90, 56.884)
	3400	3400	1700	(90, 50.7)	(90, 50.543)
	3700	3700	1850	(90, 48.3)	(90, 49.392)
	3900	3900	1950	(90, 49.0)	(90, 49.381)
	4450	4450	2225	(90, 51.6)	(90, 51.772)
	4950	4950	2475	(90, 56.3)	(90, 56.543)
	5350	5350	2675	(90, 62.8)	(90, 62.227)
	5550	5550	2775	(90, 66.0)	(90, 65.916)
	5750	5750	2875	(90, 69.1)	(90, 70.508)
	5900	5900	2950	(90, 71.4)	(90, 75.006)
SHG (YZ: <i>eo</i>)	2542.7	2542.7	1371.35	(35.4, 90)	(36.452, 90)
	2552.7	2552.7	1276.35	(34.0, 90)	(34.684, 90)
	2570.4	2570.4	1285.2	(31.0, 90)	(31.508, 90)
	2587	2587	1293.5	(28.7, 90)	(28.435, 90)
	2602.3	2602.3	1301.15	(25.9, 90)	(25.481, 90)
	2606.7	2606.7	1303.35	(25.1, 90)	(24.592, 90)
	2631.4	2631.4	1315.7	(19.6, 90)	(19.211, 90)
DFG (XY: <i>eoe</i>)	6585.14	872.240	770.220	(90, 42)	(90, 42.170)
	6623.95	865.801	765.716	(90, 42)	(90, 42.145)
	6719.87	850.443	754.905	(90, 42)	(90, 42.076)
	6762.44	843.761	750.162	(90, 42)	(90, 42.046)
	6832.63	833.187	742.629	(90, 42)	(90, 41.992)
	6899.92	822.391	734.810	(90, 42)	(90, 41.967)
	6989.56	810.827	726.544	(90, 42)	(90, 41.863)

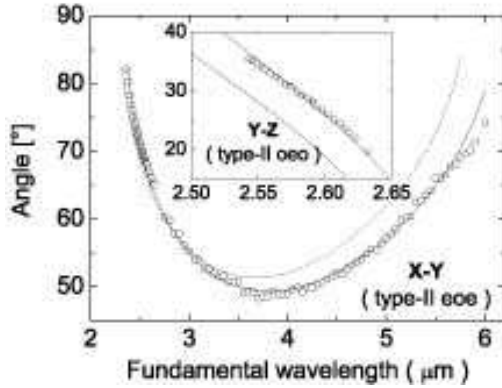
^a $1/\lambda_1 + 1/\lambda_2 = 1/\lambda_3$ with $\lambda_1 \geq \lambda_2 > \lambda_3$.^bIn degree.

FIG. 8: Phase-matching angles for type-II (*eoe* or *oe*) SHG in the X-Y principal plane (main frame) and type-II (*eo* or *eo*) SHG in the Y-Z plane (inset frame) of LIS. The fundamental source for $\lambda < 2.65 \mu\text{m}$ ($\lambda > 2.75 \mu\text{m}$, respectively) is the idler wave of a Nd:YAG-pumped nanosecond LiNbO₃ parametric oscillator (the frequency-doubled radiation from a Free-Electron Laser). The symbols refer to experiments while the solid lines are calculated from Eqs.(21)-(23). The dashed lines are computed from the Sellmeier equations of Refs. [56].

B. Thermo-optic dispersion relations

The thermo-optic coefficients β_j [Eq. (10)] are functions of both temperature T (in $^{\circ}\text{C}$) and wavelength λ (in μm). In analogy with the index dispersion equations at room-temperature (see previous subsection) the parameters $a_k(\lambda)$ ($k = 1, 2$) in Table I are fitted according to the following two-pole functional form,

$$a_k(\lambda) = C_{0,k} + \frac{C_{1,k}}{\lambda^2 - \lambda_{01,k}^2} + \frac{C_{2,k}}{\lambda^2 - \lambda_{02,k}^2}. \quad (25)$$

Table V compiles the fitting parameters $C_{0,k}, C_{1,k}, C_{2,k}, \lambda_{01,k}$ and $\lambda_{02,k}$. According to the definition $\beta_j = \frac{1}{n_j} \frac{dn_j}{dT}$, the index of refraction at a given temperature T will be given by

$$\begin{aligned} \frac{n(\lambda, T)}{n(\lambda, T_0)} &= \exp \left[a_1(\lambda)(T - T_0) + a_2(\lambda) \frac{(T - T_0)^2}{2} \right] \\ &\simeq 1 + a_1(\lambda)(T - T_0) + a_2(\lambda) \frac{(T - T_0)^2}{2} \end{aligned} \quad (26)$$

where $T_0 = 20^{\circ}\text{C}$ and $n(\lambda, T_0)$ is given by Eqs.(21)-(23).

These thermo-optic dispersion relations will have to be refined by experimental temperature phase-matching data in the future. Relations (25) with the constant values in Table V would provide a suitable basis for such

TABLE V: Fitting parameters describing the thermal and wavelength dependence of the principal thermo-optic coefficients of LIS, according to Eqs.(??)-(25).

$a_k(\lambda)$	p_i	C_0	C_1	C_2	λ_{01}	λ_{02}
a_1	X	2.899680×10^{-5}	0.2033761×10^{-5}	297.0535×10^{-5}	0.3475601	14.86755
	Y	2.478267×10^{-5}	0.2612463×10^{-5}	122.3207×10^{-5}	0.3391212	13.91854
	Z	3.315830×10^{-5}	0.2555208×10^{-5}	364.9813×10^{-5}	0.3451539	15.44113
a_2	X	1.987083×10^{-8}	0.1860292×10^{-8}	250.0777×10^{-8}	0.3886392	14.25991
	Y	0.1523235×10^{-8}	0.2601335×10^{-8}	-191.8712×10^{-8}	0.3969192	14.79803
	Z	$-0.6564806 \times 10^{-8}$	0.4291068×10^{-8}	-343.1015×10^{-8}	0.3435849	14.94811

a refit procedure. They predict a FWHM temperature acceptance of $\Delta TL = 248^\circ\text{C}\cdot\text{cm}$ (L : crystal length) at room temperature for the type-II (eoe) SHG at the fundamental $\lambda = 2.5\mu\text{m}$ in the X-Y plane. Hence LIS is expected to be very stable against self-induced thermal effects. As a counterpart, its temperature tunability is expected to be somewhat limited. However for the DFG of near-IR sources ($\lambda_3 = 754.905\text{ nm}$, $\lambda_2 = 850.443\text{ nm}$, see Table IV), the FWHM temperature acceptance is predicted to be only $\Delta TL = 46^\circ\text{C}\cdot\text{cm}$.

VII. PHASE-MATCHING INVESTIGATIONS

A. Effective nonlinearity and Hobden classification

The phase-matching loci and the effective nonlinearity for LIS will be analyzed in the XYZ-principal optic axis frame, but the tensor elements of the nonlinear susceptibility are defined traditionally, in accordance with ANSI/IEEE Std 176-1987 [36], in the *abc*-crystallographic frame where c is the polar two-fold axis as in Ref. [9]. The chosen convention $n_X < n_Y < n_Z$ in order to have the two optic axes in the X-Z principal plane affects therefore the expressions for the effective second order nonlinearity d_{eff} .

The general form of the contracted $\mathbf{d}^{(2)}$ tensor for the orthorhombic class *mm2* reads as

$$\mathbf{d}^{(2)} = \begin{pmatrix} 0 & 0 & 0 & 0 & d_{15} & 0 \\ 0 & 0 & 0 & d_{24} & 0 & 0 \\ d_{31} & d_{32} & d_{33} & 0 & 0 & 0 \end{pmatrix}. \quad (27)$$

For an arbitrary propagation direction assuming collinear interaction and neglecting the spatial walk-off effect analytical expressions for d_{eff} can be derived in our conventions from the general formulae presented by

Dmitriev *et al* [60],

$$\begin{aligned} d_{\text{eff}}^{ssf} = & 2 d_{15} \sin \theta \cos \delta (\cos \theta \sin \varphi \sin \delta - \cos \varphi \cos \delta) \\ & \times (\cos \theta \sin \varphi \cos \delta + \cos \varphi \sin \delta) \\ & + 2 d_{24} \sin \theta \cos \delta (\cos \theta \cos \varphi \cos \delta - \sin \varphi \sin \delta) \\ & \times (\cos \theta \cos \varphi \sin \delta + \sin \varphi \cos \delta) \\ & + d_{31} \sin \theta \sin \delta (\cos \theta \sin \varphi \cos \delta + \cos \varphi \sin \delta)^2 \\ & + d_{32} \sin \theta \sin \delta (\cos \theta \cos \varphi \cos \delta - \sin \varphi \sin \delta)^2 \\ & + d_{33} \sin^3 \theta \cos^2 \delta \sin \delta \end{aligned} \quad (28)$$

and

$$\begin{aligned} d_{\text{eff}}^{fff} = & d_{\text{eff}}^{ssf} \\ = & - d_{15} [\sin \theta \cos \delta (\cos \theta \sin \varphi \sin \delta - \cos \varphi \cos \delta)^2 \\ & + \sin \theta \sin \delta (\cos \theta \sin \varphi \sin \delta - \cos \varphi \cos \delta) \\ & \times (\cos \theta \sin \varphi \cos \delta + \cos \varphi \sin \delta)] \\ & - d_{24} [\sin \theta \cos \delta (\cos \theta \sin \varphi \sin \delta + \sin \varphi \cos \delta)^2 \\ & + \sin \theta \sin \delta (\cos \theta \cos \varphi \cos \delta - \sin \varphi \sin \delta) \\ & \times (\cos \theta \cos \varphi \sin \delta + \sin \varphi \cos \delta)] \\ & - d_{31} \sin \theta \sin \delta (\cos \theta \sin \varphi \sin \delta - \cos \varphi \cos \delta) \\ & \times (\cos \theta \sin \varphi \cos \delta + \cos \varphi \sin \delta) \\ & - d_{32} \sin \theta \sin \delta (\cos \theta \cos \varphi \cos \delta - \sin \varphi \sin \delta) \\ & \times (\cos \theta \cos \varphi \sin \delta + \sin \varphi \cos \delta) \\ & - d_{33} \sin^3 \theta \sin^2 \delta \cos \delta \end{aligned} \quad (29)$$

for type-I and type-II phase-matching, respectively, where the superscripts "s" and "f" stand for the "slow" and "fast" eigenmodes of polarization and their sequence follows the usual convention $\lambda_1 \lambda_2 \lambda_3$ with $\lambda_1 \geq \lambda_2 > \lambda_3$. The angle δ whose introduction simplifies the expressions and which is determined from

$$\tan 2\delta = \frac{\cos \theta \sin 2\varphi}{\cot^2 V_Z \sin^2 \theta + \sin^2 \varphi - \cos^2 \theta \cos^2 \varphi} \quad (30)$$

($0 < 2\delta < \pi$) defines the polarization directions of the slow and fast waves which are orthogonal to each other. It is the angle between the polarization direction of the slow wave and the plane of propagation containing the

principal Z-axis. An approach for the generalization of the d_{eff} expressions in the case of collinear interactions taking into account the spatial walk-off can be found in Ref. [61].

In the principal planes the expressions for d_{eff} (28)-(29) are reduced to:

$$d_{\text{eff}}^{oeo} = d_{\text{eff}}^{oeo} = -(d_{24} \sin^2 \varphi + d_{15} \cos^2 \varphi) \quad (\text{X-Y plane}) \quad (31)$$

$$d_{\text{eff}}^{ooo} = d_{\text{eff}}^{ooo} = -d_{24} \sin \theta \quad (\text{Y-Z plane}) \quad (32)$$

$$d_{\text{eff}}^{oeo} = +d_{31} \sin \theta \quad (\text{X-Z plane, } \theta < V_Z) \quad (33)$$

$$d_{\text{eff}}^{oeo} = d_{\text{eff}}^{oeo} = -d_{15} \sin \theta \quad (\text{X-Z plane, } \theta > V_Z) \quad (34)$$

with superscripts "o" and "e" denoting the ordinary and extraordinary beams. LIS behaves as an optically negative uniaxial crystal in the X-Y and X-Z (for $\theta < V_Z$) planes and as an optically positive uniaxial crystal in the Y-Z and X-Z (for $\theta > V_Z$) planes. Assuming the Kleinman symmetry condition to hold then $d_{15} = d_{31}$ and $d_{24} = d_{32}$.

The phase-matching loci for collinear SHG can be categorized using the classification of Hobden [62]. Our calculations based on the relatively simple transcendental equations derived by Yao *et al* [63], predict that no phase-matched SHG is possible below 1617 nm. LIS enters Hobden class 13 at 1617 nm, class 11 at 1783 nm, class 10 at 2353 nm, and class 9 at 2675 nm, then it goes back to class 10 at 5493 nm, to class 11 at 6111 nm, to class 13 at 8224 nm, and finally no SHG phase-matching is possible again above 8710 nm. These transitional fundamental wavelengths correspond to propagation directions along the Y - or along the Z - principal axes (noncritical phase-matching) either for the *ssf* or the *fsf* (*fff*) polarization configurations.

Figs. 9a,b illustrate the different classes for SHG in LIS at several representative fundamental wavelengths. The surface of the unit sphere is projected onto the X-Z plane of the crystal. The direction of the wave vectors of the interacting waves for phase-matching as given by their interception with the surface of the unit sphere is plotted. The stereographic projection of the first octant is presented only but the loci in the other octants can be obtained by mirror reflections across the principal planes. We do not present plots of the angle δ which can be easily calculated from Eq.(30). Its dispersive properties (determined by the angle V_Z) lead to slightly different values at the three interacting wavelengths but normally the effect on the conversion efficiency can be neglected. Qualitative arguments relating the spatial walk-off (magnitude and direction) to the topology depicted in Fig. 9 can be found in Ref. [35]. The calculation of the spatial walk-off for an arbitrary propagation direction is beyond the scope of this paper but several works provide suitable approaches to this aim [64, 65, 66, 67]. Analytical approaches for the estimation of acceptance parameters based on the small-signal approximation in the general case of biaxial crystals can be found in Ref. [65, 68]. We note here only, that since the angle V_Z for LIS is not far from 90°

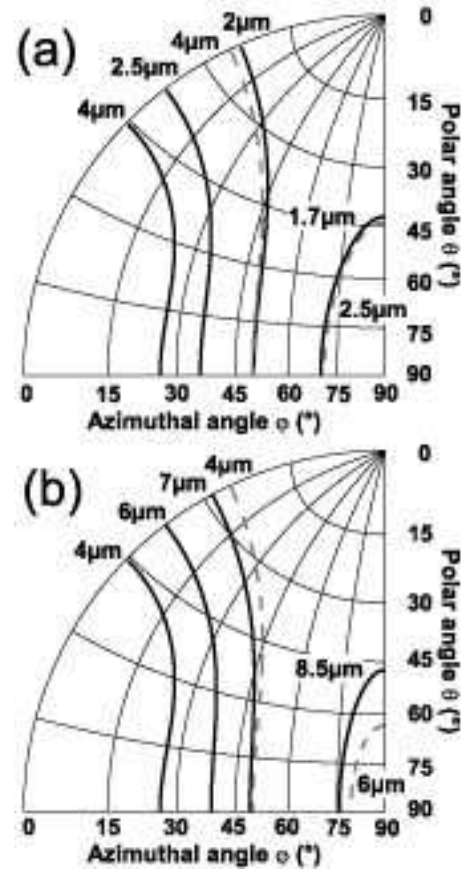


FIG. 9: (a)-(b): Stereographic projections of the SHG in the first octant of LIS calculated for wavelengths representative of the Hobden classes. Type-I (*ssf*) interaction (solid lines) and type-II (*fsf*, *fff*) interactions (dashed lines). The wavelength annotations refer to the fundamental ones.

the dispersive properties and in particular the spectral acceptance are not expected to be substantially modified by propagation outside the principal planes. Fig. 9 indicates that double solutions for the angles exist (e.g. for Hobden's class 9) which is equivalent to the existence of points outside the principal planes where $\partial\varphi/\partial\theta = 0$ holds. This means that noncritical phase-matching in one direction can also occur outside the principal planes (e.g. at $\varphi = 26.7^\circ$, $\theta = 74.35^\circ$ for *ssf* type SHG at $4\mu\text{m}$).

B. SHG in principal planes

The SHG phase-matching directions in the principal planes are shown in the lower part of Fig. 10. The two first panels (X-Y) and (Y-Z) in the bottom part correspond respectively to the experimental phase-matching plots in the main and inset panels of Fig. 8. The transitional wavelengths enumerated above can be easily identified there. The SHG ranges where $d_{\text{eff}} \neq 0$ are 1783-8224 nm for type-I (*oeo*) phase-matching in the X-Z plane, 2353-6111 nm for type-II (*oeo*) phase-matching

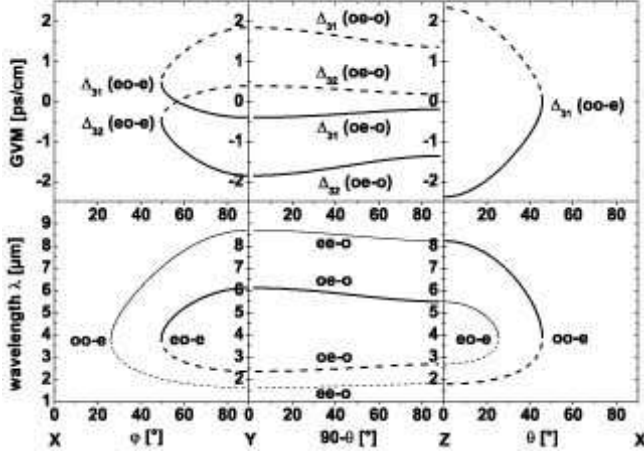


FIG. 10: SHG phase-matching in the principal planes of LIS. Thick lines in the lower part show fundamental wavelengths for which $d_{\text{eff}} \neq 0$ and thin lines indicate cases where d_{eff} vanishes. The inverse group velocity mismatch GVM ($\Delta_{31} = v_3^{-1} - v_1^{-1}$ and $\Delta_{32} = v_3^{-1} - v_2^{-1}$ where v_1, v_2, v_3 denote the group velocities $\partial\omega_i/\partial k_i$ at λ_1, λ_2 , and λ_3) is shown in the upper part for the cases where $d_{\text{eff}} \neq 0$. The solid (dashed) lines correspond to the branch with longer (shorter) wavelengths.

in the X-Y plane, and 2353-2675 nm and 5493-6111 nm for type-II (o-o) phase-matching in the Y-Z plane. We observe an interesting feature in this crystal: the SHG limits with $d_{\text{eff}} \neq 0$ are larger for propagation *outside* the principal planes where type-I phase-matching down to 1617 nm and up to 8710 nm is possible. Under the convention $n_X < n_Y < n_Z$ the largest birefringence and consequently the shortest SHG wavelength is obviously achieved for type-I interaction and propagation along the Y-axis. However, in LIS when the Y-axis is approached in the principal planes X-Y or Y-Z d_{eff} for type-I interaction vanishes and this is true also for the limiting case of propagation along the Y-axis. This is the reason why propagation outside the principal planes can be used e.g. to shorten the SHG lower wavelength limit (Fig. 9). A similar situation is known to exist and has been experimentally verified in KTP [69].

It is seen from Fig. 10 that in the Y-Z plane the type-II interaction is quasi angle-noncritical (but wavelength-critical, see inset of Fig. 8) which ensures a large acceptance angle and a small walk-off angle. In contrast, type-I interaction in the X-Z plane and type-II interaction in the X-Y plane have regions of quasi-wavelength-noncritical phase-matching ($\partial\Phi/\partial\lambda \sim 0$) centered at 3889 nm and 3803 nm, respectively (Fig. 10, see also Fig. 8). Letting $\Phi = \varphi$ or θ , the walk-off angles in the upper panels of Fig. 11 are calculated using the simplified formula $\tan \rho_i = [n_i^e(\Phi)]^{-1} \partial n_i^e / \partial \Phi$ valid for uniaxial crystals, where the subscript $i = 1, 2, 3$ is associated with wavelength λ_i ($\lambda_3^{-1} = \lambda_2^{-1} + \lambda_1^{-1}$) and $n_i^e(\Phi)$ is the extraordinary index of refraction of the walking-off wave as given by the uniaxial analogy in the principal planes. We

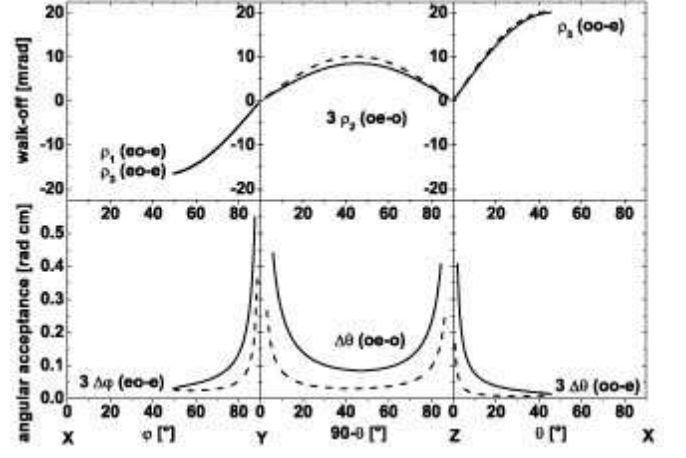


FIG. 11: SHG internal angular acceptance (bottom) and walk-off angles (top) in the principal planes of LIS. Thick solid lines correspond to the branches with longer wavelengths from Fig. 10 and thick dashed lines correspond to the branches with shorter wavelengths. Only the cases with $d_{\text{eff}} \neq 0$ are included.

preserved its sign which is in accordance with the corresponding phase-matching angles i.e. a positive value of the walk-off means that the Poynting vector is at an angle larger than the phase-matching angle and vice-versa. Note that the walk-off is very similar for the two branches of the solution for phase-matching in all three principal planes. In the X-Y plane these branches and the two different walk-off parameters (we have here two extraordinary waves) are almost undistinguishable. The maximum walk-off amounts to $\rho_3 = +1.15^\circ$ in the X-Z plane for SHG at 3889 nm.

The acceptance angle is evaluated from the phase velocity mismatch $\Delta k(\delta\Phi)$ due to an angular deviation $\delta\Phi = \Phi - \Phi_{\text{PM}}$ of the wavevectors around the nominal phase-matched direction Φ_{PM} . A Taylor expansion of Δk leads to

$$\Delta k(\delta\Phi) = \gamma_{\text{CPM}} \delta\Phi + \gamma_{\text{NCPM}} (\delta\Phi)^2 + \dots \quad (35)$$

where $\gamma_{\text{CPM}} = [\partial(\Delta k)/\partial\Phi]_{\Phi=\Phi_{\text{PM}}}$ vanishes for non-critical phase-matching (NCPM, i.e. for $\Phi = 0, 90^\circ$) and $\gamma_{\text{NCPM}} = \frac{1}{2} [\partial^2(\Delta k)/\partial\Phi^2]_{\Phi=\Phi_{\text{PM}}}$. The acceptance angle, defined as the bandwidth at FWHM of the $\text{sinc}^2(\Delta k L/2)$ phase-mismatch function, is given by $\Delta\Phi = 2.784/|\gamma_{\text{CPM}}|L$ for a critical phase-matching (CPM), while for NCPM it is $\Delta\Phi = |2.784/\gamma_{\text{NCPM}}L|^{1/2}$. The lower panels of Fig. 11 display the acceptance angles (for a length $L = 1$ cm) in the three principal planes. The acceptance curves, computed with γ_{CPM} only in the expansion (35), are interrupted near non-criticality at maximum values corresponding to the ones calculated for $L = 1$ cm using γ_{NCPM} only. Although that type of presentation in Fig. 11 is not very accurate in these limits we still prefer it since it permits the results to be presented as scalable with re-

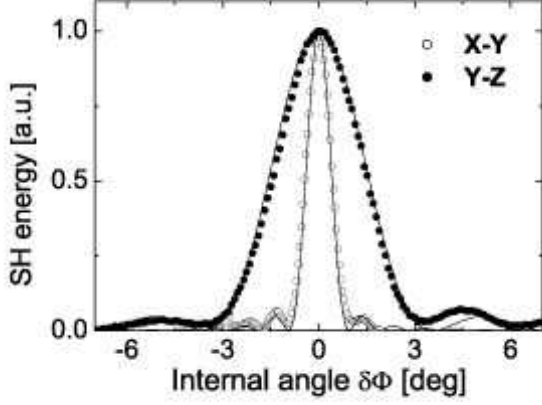


FIG. 12: Experimental angular tuning curves for type-II SHG of $\lambda = 2590$ nm in the X-Y plane (at $\Phi_{PM} \equiv \varphi_{PM} = 66.2^\circ$, blank circles) and in the Y-Z plane (at $\Phi_{PM} \equiv \theta_{PM} = 27.9^\circ$, black circles). The larger acceptance angle in the Y-Z plane is due to the much smaller $\Delta n_{Y-Z} = -0.007$ birefringence as compared with $\Delta n_{X-Y} = -0.035$ (Fig. 6). The walk-off angles are $\rho_1 \simeq \rho_3 = 12.2$ mrad (X-Y), $\rho_2 = 2.8$ mrad (Y-Z). The crystal lengths are $L = 6$ mm (sample LIS(1) used in X-Y) and $L = 7$ mm (sample LIS(2) used in Y-Z plane), see Subsection VIII A. The fundamental beam (diameter $2w_0 \approx 2.6$ mm) is the idler output of a ns Nd:YAG-pumped LiNbO₃ OPO.

spect to the crystal length L (simultaneous consideration of both derivatives would not allow this). The experimental comparison of type-II SHG acceptance angles in the Y-Z and X-Y planes is shown with symbols in Fig. 12, for $\lambda = 2590$ nm. The solid lines depict the plane-wave $\text{sinc}^2(\Delta k L/2)$ phase-mismatch tuning functions computed with the first-order term in Eq.(35), with $\gamma_{CPM}(\theta_{PM}) = (\pi/\lambda)[n_2^e \rho_2]_{\theta_{PM}} = 7.2 \times 10^{-3} \mu\text{m}^{-1}$ (type-II (*oeo*) SHG in the Y-Z plane) and $\gamma_{CPM}(\varphi_{PM}) = (\pi/\lambda)[2n_3^e \rho_3 - n_1^e \rho_1]_{\varphi_{PM}} = 3.17 \times 10^{-2} \mu\text{m}^{-1}$ (type-II (*oeo*) SHG in the X-Y plane). The perfect match of the theoretical curves with the experimental symbols highlights both the accuracy of the dispersion data and the single-domain feature of the samples used.

The chosen presentation of the inverse group velocity mismatch in the upper part of Fig. 10 is equivalent to the spectral acceptance $\Delta\nu$ but contains the sign as an additional information. In the simplest cases of type-I SHG or degenerate DFG we have e.g. $\Delta\nu L = 0.886/|\Delta_{31}|$ and the gain bandwidth in optical parametric amplification assuming a narrow-band pump wave at λ_3 is inversely proportional to $|\Delta_{21}| = |1/v_2 - 1/v_1|$. The two parameters Δ_{31} and Δ_{32} vanish at 3889 nm in the X-Z plane which means large spectral acceptance for the SHG of short pulses where the second derivative of the wavevector-mismatch comes into play. The situation is different for type-II interaction in the X-Y plane: here $\Delta_{32} = -\Delta_{31}$ at 3803 nm, at 2915 nm Δ_{32} vanishes and at 4946 nm Δ_{31} vanishes but in none of these cases an

extremum of the spectral acceptance occurs because in type-II SHG of short pulses all three waves should be considered as broad-band. Thus long crystals can be used to increase the conversion efficiency for type-I SHG in the X-Z plane near 3889 nm even at femtosecond pulse durations. For type-II SHG of femtosecond pulses near 3803 nm in the X-Y plane the second harmonic will not be lengthened either because the temporal walk-off between the two polarizations of the fundamental wave will limit the interaction length, but consequently the conversion efficiency will be low.

C. Sum-and-difference frequency mixing

Type-I phase-matching in the X-Z plane for non-degenerate three-wave interactions (sum- and difference-frequency mixing as well as optical parametric generation, amplification and oscillation) is presented in Fig. ?? where two branches of the solution can be seen. The whole transparency range of LIS can be covered for $0^\circ < \theta < 40^\circ$ in the X-Z plane but d_{eff} increases with the phase-matching angle θ . Note that $d_{\text{eff}} = 0$ for NCPM ($\theta = 0^\circ$) and that the situation $\theta > V_Z$ (Eq. 34) is never reached. At larger angles θ we observe a retracing behavior in the left branch: e.g. in the case of OPO, one and the same pump wavelength λ_3 corresponds to two pairs (λ_1, λ_2) of signal-idler wavelengths (curve 5). In this region the spectral acceptance is very large. Thus for $\theta = 40^\circ$ (left branch of curve 5), $\lambda_3 = 900$ nm and $\lambda_2 = 1150$ nm all three group velocities are very close: at the point where $\Delta_{31} = 0$ we have $\Delta_{32} = 23$ fs/mm. This means that this phase-matching configuration is especially suitable for frequency conversion of femtosecond pulses. In optical parametric amplifiers (OPA's) this advantage can be utilized, however, only in combination with a control of the spectral bandwidth through the seed signal. In the regions near the degeneracy points (SHG points) we have on the other hand $\Delta_{21} = 0$ but the wave at λ_3 can have in general a different group velocity. Such a regime is attractive for broadband parametric amplification in the field of a narrow-band pump pulse as in the case of chirped pulse optical parametric amplification [70]. For femtosecond-laser based frequency metrology applications [71], this phase-matching when implemented in a synchronously-pumped OPO would provide a wide frequency comb grid spanning the $10 - 12 \mu\text{m}$ region useful for high precision spectroscopy of spherical reference standard molecules. Increasing the phase-matching angle (curve 6 for $\theta = 45^\circ$ in Fig. ??) the two branches merge into a closed contour and we approach the point where SHG phase-matching only for a single wavelength is possible (see Fig. 10) and all three group velocities are again very close but the tunability in that case is very limited.

The curves for type-II phase-matching in the X-Y plane (Fig. 13) have a completely different shape. The two branches of the solution are represented by curves of

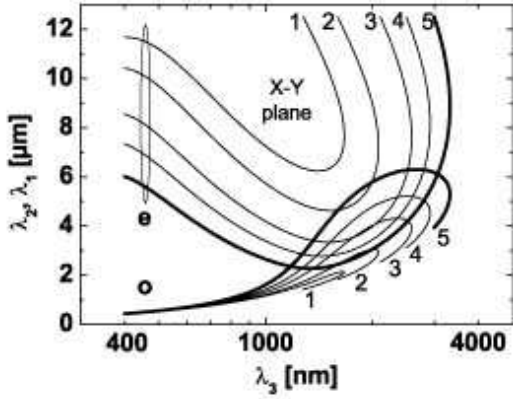


FIG. 13: Type-II (*eoe* and *oee*) phase-matching for sum- and difference-frequency generation in the X-Y plane of LIS and several values of the azimuthal angle φ : 35° (lines 1), 40° (lines 2), 50° (lines 3), 60° (lines 4) and 90° - NCPM (thick lines 5). The curves are terminated at the left and top side by the transparency range of the crystal.

opposite curvature which can cross at two points where phase-matching for degenerate DFG or SHG occurs. With decreasing phase-matching angle these branches separate and a single crossing point is reached (see the curves 3 for $\varphi = 50^\circ$) which corresponds to the single SHG solution in Fig. 10. For yet smaller angles no crossing occurs and the degeneracy point is not reached. For all phase-matching curves presented we observe again a retracing behavior at longer λ_3 : for each λ_3 two couples (λ_1, λ_2) are phase-matched. At the point where these two pairs merge into one (at the maximum λ_3 permitting phase-matching) the waves at λ_1 and λ_2 have equal group velocities and similarly to the case discussed for Fig. ?? broadband parametric amplification with a narrow-band pump wave can be realized. The deviation from the pump group velocity remains, however, essential. Thus e.g. at $\varphi = 90^\circ$ and $\lambda_3 = 3310$ nm, $\Delta_{21} \simeq 0$ and $\Delta_{31} \simeq \Delta_{32} \simeq -1.65$ ps/cm. Improved pump group-matching at this point occurs when decreasing the phase-matching angle φ in accordance with Fig. 10.

Comparing Fig. 13 to Fig. ?? we note that at relatively short λ_3 (e. g. 1064 nm) full tunability with a fixed crystal cut is achievable only in the X-Z principal plane. The group velocity mismatch depends on the specific wavelengths chosen. At $\lambda_3 = 1064$ nm (a case interesting for parametric down-conversion) $\Delta_{21}(X-Z) < \Delta_{21}(X-Y)$ up to $\lambda_1 = 10 \mu\text{m}$. This means that in this practical wavelength range type-II phase-matching in the X-Y plane is more advantageous for the development of narrow-band parametric generators or oscillators.

Our analysis of the phase-matching properties of LIS is just a first order approximation because it was based on the small signal limit where saturation is neglected. We considered also only collinear interactions. Non-collinear interactions attracted recently great interest because in addition to the possibility to improve the tunability, to

spatially separate the beams, and to compensate for the spatial walk-off, this can considerably reduce the group velocity mismatch [72]. The latter is very promising for short pulse interactions. Explicit expressions for non-collinear phase-matching in the principal planes of a biaxial crystal can be found in Ref. [73] and calculations of non-collinear group velocity matching for arbitrary wave vector directions in Ref. [68].

VIII. SECOND-ORDER NONLINEAR COEFFICIENTS

There has been only one characterization study of the nonlinear properties of LIS made by Boyd *et al* in the early seventies [9]. The samples used then were of limited size and poor quality, and besides their results were derived only from non-phase matched SHG at $10.6 \mu\text{m}$ (wedge technique). Further their measurements were performed relative to the nonlinearity of GaAs, that was several times corrected during the past years. So it is important to confirm or to correct these previous results using phase-matched second-order interactions on mature samples of adequate size.

The elements d_{ij} of the nonlinear tensor (27) have been determined from the measurement of the SHG efficiency of various laser sources, using either type-I or type-II interactions in the principal planes of LIS and also out of them. Two kinds of measurements have been performed: in one kind (Subsection A), the source is the idler output (in the range $2.4 - 2.6 \mu\text{m}$) of a 12-ns pulsewidth, 10-Hz repetition rate, type-I LiNbO₃-OPO [19]. Long samples were used, and hence the residual absorption and the beam walk-off effect, as well as the focusing effects, have to be taken into account to derive the nonlinear coefficients. The second independent series of SHG experiments (Subsection B) used femtosecond pulses and very thin oriented samples. This allows to neglect the effect of absorption and beam walk-off and focusing effects, the data analysis in the low-depletion limit being derived from the standard plane-wave SHG theory.

A. Measurements based on Gaussian beam SHG theory

In order to remain in the low pump depletion limit, the peak on-axis fundamental intensity used was below 10 MW/cm^2 , and the maximum idler energy of the LiNbO₃-OPO was 10 mJ at $\lambda = 2590$ nm. The spectral linewidth of the idler was below 15 GHz, and the transverse beam profile resembled a Gaussian. Three thick samples of different coloration (rose and yellowish) were used in conjunction with weak focusing producing Gaussian beam waist of either $w_0 \sim 1 \text{ mm}$ or $w_0 \sim 1.3 \text{ mm}$. Sample LIS(1) was rose-annealed, cut at ($\varphi = 66.5^\circ, \theta = 90^\circ$) for type-II (*eoe*) SHG in the X-Y plane, with dimensions $4 \times 4 \times 6 \text{ mm}^3$ ($L = 6 \text{ mm}$). Sample LIS(2) was yellowish

(as-grown), cut at $(\varphi = 90^\circ, \theta = 28^\circ)$ for type-II (*oeo*) SHG in the Y-Z plane, with dimensions $4 \times 4 \times 7 \text{ mm}^3$ ($L = 7 \text{ mm}$). LIS(1) and LIS(2) were the same samples already used in Subsection VI A, see Fig. 8 and also Fig. 12. Sample LIS(3) had almost identical cut as LIS(1) ($\varphi = 66^\circ, \theta = 90^\circ$), but was of yellowish tinge and with dimensions $4 \times 4 \times 5 \text{ mm}^3$ ($L = 5 \text{ mm}$). We have checked that, as the linear dispersion data, the nonlinear coefficients do not significantly depend on coloration when the additional absorption effect of the yellow samples was taken into account. For typical pump energy $E_\omega = 1 \text{ mJ}$ and $w_0 = 1.3 \text{ mm}$, LIS(2) yielded $E_{2\omega} = 2.5 \mu\text{J}$, while LIS(1) yielded $E_{2\omega} = 11 \mu\text{J}$ and LIS(3), $E_{2\omega} = 7 \mu\text{J}$. The difference between the efficiencies of LIS(1) and LIS(3) was mainly due to the much stronger second harmonic absorption of the latter ($\alpha_{2\omega} = 0.27 \text{ cm}^{-1}$) [44]. For LIS(1), the residual fundamental and harmonic absorption amounted to $\alpha_{\omega, 2\omega} = 0.05 - 0.06 \text{ cm}^{-1}$ while for LIS(2) $\alpha_{\omega, 2\omega} \simeq 0.6 \text{ cm}^{-1}$ [44].

The measurements were performed relatively to a dual-band anti-reflection-coated KTP sample with $L = 5.93 \text{ mm}$, cut at $(\varphi = 0^\circ, \theta = 56.4^\circ)$ for SHG of $\lambda = 2.53 \mu\text{m}$ in the X-Z plane. The measured nonlinear coefficient of KTP was $d_{24} = 2.3 \pm 0.2 \text{ pm/V}$ [74] and served as a reference, without having to correct for dispersion since the measurement wavelength is almost identical to that used for LIS. We only corrected for the residual absorption loss ($\alpha_\omega = 0.068 \text{ cm}^{-1}$ at $2.59 \mu\text{m}$) of this KTP sample, due to OH^- band [74]. According to the Gaussian beam SHG theory in the nanosecond pulse regime, the effective nonlinearity in the absence of depletion scales as [75]

$$d_{\text{eff}}^2 = \Gamma_{\text{SH}} \frac{\tau_\omega^2}{\tau_{2\omega}} \frac{c\epsilon_0 n^2 \lambda^3}{16\pi^2 L h} \quad (36)$$

where $\Gamma_{\text{SH}} = E_{2\omega}/E_\omega^2$ is the pulse energy conversion efficiency (in unit of J^{-1}), n is the average index of refraction at fundamental and harmonic wavelengths and h is the walk-off-focusing function that accounts for diffraction, absorption and beam-walk-off effects. The exact expression of h for type-II interaction can be found in Ref. [76]. The second harmonic pulse duration was taken as $\tau_{2\omega} \simeq \tau_\omega/\sqrt{2}$. In the nanosecond regime and for the given crystal lengths, group-velocity mismatch can be safely neglected in SHG. The advantage of measuring the LIS coefficient relative to a reference material stems from the fact that it is neither necessary to evaluate the absolute energies nor to take into account the loss due to the numerous filter sets used to isolate the fundamental and second harmonic field, since from Eq.(36), the ratio of the two d_{eff} 's scales as

$$\frac{d_{\text{eff}}^2(\text{LIS})}{d_{\text{eff}}^2(\text{KTP})} = \frac{\Gamma_{\text{SH}}(\text{LIS})}{\Gamma_{\text{SH}}(\text{KTP})} \frac{n^2(\text{LIS})}{n^2(\text{KTP})} \frac{L(\text{KTP})}{L(\text{LIS})} \frac{h(\text{KTP})}{h(\text{LIS})}. \quad (37)$$

The efficiencies Γ_{SH} were derived from the linear fit of the plot of $E_{2\omega}$ versus E_ω^2 , for fundamental energies ranging from 0 to 5 mJ [44]. The results of the data analysis,

averaged over the two waist values, are the following:

$$d_{\text{eff}}[\text{LIS}(2)] = 1.36 (\pm 15\%) d_{\text{eff}}(\text{KTP}), \quad (38)$$

$$d_{\text{eff}}[\text{LIS}(1)] = 3.05 (\pm 15\%) d_{\text{eff}}(\text{KTP}), \quad (39)$$

$$d_{\text{eff}}[\text{LIS}(3)] = 3.15 (\pm 15\%) d_{\text{eff}}(\text{KTP}). \quad (40)$$

The rather large uncertainties are mainly due to the uncertainty in the absorption coefficients through the evaluation of the h focusing functions. Given that $d_{\text{eff}}(\text{KTP}) = d_{24} \sin \theta$ ($\theta = 58.7^\circ$ at $\lambda = 2590 \text{ nm}$), from (38) and (32) one derives $d_{24}(\text{LIS}) = 5.73 \pm 20\% \text{ pm/V}$. The two last relations (39)-(40) were averaged to yield, using (31) and the determined value of d_{24} , $d_{15}(\text{LIS}) = 7.94 \pm 20\% \text{ pm/V}$. The ratio of the two nonlinear coefficients is hence found to be $d_{24}/d_{15} = 0.72$.

B. Measurements based on femtosecond SHG

The SHG experiments with femtosecond pulses were performed also in the low depletion limit for the fundamental in order to avoid complications from saturation effects and spatial effects across the beam cross section. The coefficient d_{31} was estimated by type-I SHG in the X-Z plane from Eq.(33), once it was known it was used for the determination of d_{24} from type-II SHG in the X-Y plane using Eq.(31) and assuming Kleinman symmetry to hold (i.e. $d_{15} = d_{31}$). Finally the diagonal element d_{33} was measured by type-I SHG outside the principal planes using Eq.(28) and the already determined off-diagonal components of the $\mathbf{d}^{(2)}$ -tensor, again assuming Kleinman symmetry. Note that a similar strategy was used previously to determine d_{33} of KTP by phase-matched SHG [77] and as outlined there the error in the determination of this diagonal element is normally larger since it accumulates the uncertainties of the other coefficients. Alternatively the plane Y-Z could be used for determination of d_{24} as done in the previous subsection, however, the spectral tunability is very narrow in this principal plane (see Fig. 10) which is not adequate for measurements with broadband femtosecond pulses.

All three LIS samples used here were annealed and rose in colour, had an aperture of $4 \times 5 \text{ mm}^2$ and were 0.2 mm thick. They were cut at $(\varphi = 0^\circ, \theta = 34^\circ)$ [LIS(4)], $(\varphi = 59^\circ, \theta = 90^\circ)$ [LIS(5)], and $(\varphi = 30^\circ, \theta = 44^\circ)$ [LIS(6)], respectively. The small thickness allows to neglect absorption or scattering losses, the focusing effects and also spatial beam walk-off effects. This measurement was also relative and we used as a reference sample an AGS crystal with the same dimensions cut at $\varphi = 45^\circ$ and $\theta = 45^\circ$ for type-I SHG. In order to minimize the error originating from the still different group-velocity mismatch the pulsewidth at the fundamental was chosen relatively large (160 fs in all cases) since LIS samples with thickness less than 0.2 mm could not be prepared with sufficient quality. This pulsewidth corresponds to spectral bandwidths of 80-90 nm. For d_{36} of AGS we used the value of 13.9 pm/V [78] which was measured at a similar wavelength ($\lambda = 2.53 \mu\text{m}$) and actually relative to

d_{24} of KTP using the same value for the latter as in the previous subsection of the present work. In the plane wave approximation and having in mind the equal fundamental energy and crystal thickness, d_{eff} of LIS was determined simply from

$$\frac{d_{\text{eff}}^2(\text{LIS})}{d_{\text{eff}}^2(\text{AGS})} = \frac{E_{2\omega}(\text{LIS})}{E_{2\omega}(\text{AGS})} \frac{[1 - R(\text{AGS})]^3}{[1 - R(\text{LIS})]^3} \frac{n^3(\text{LIS})}{n^3(\text{AGS})} \quad (41)$$

where n^3 is the product of the the three refractive indices involved, and R takes into account the Fresnel reflections at the entrance surface (twice for the fundamental) and the exit surface (second harmonic).

The femtosecond source at 1-kHz repetition rate was a KTP-based OPA which was seeded by the frequency-doubled idler of a BBO-based OPA, both OPAs being pumped by the same 800 nm, 40 fs pump source (Ti:sapphire regenerative amplifier). The 3-mm KTP used in the OPA ensured sufficiently long wavelengths that cannot be achieved by BBO. Seeding by the frequency doubled idler of the BBO-OPA was preferred against seeding by the signal wavelength for two reasons: the signal wavelengths available from the BBO-OPA were not short enough to produce idler wavelengths above 2.5 μm with the KTP-OPA, and frequency doubling in a 2-mm thick BBO crystal of the idler used for seeding resulted in temporal broadening and spectral narrowing which was a prerequisite to improve the accuracy. SHG was performed at 2330 nm with LIS(4), 2850 nm with LIS(5) and 2300 nm for LIS(6). In all cases more than 5 μJ at the fundamental were available so that it was possible to reliably measure the SHG with a large area pyroelectric detector even at low conversion efficiency. We established that up to a conversion efficiency of 20% (energy) into the second harmonic the result did not change. In the case of LIS(6) the polarization angle δ was adjusted by a He-Ne laser monitoring the polarization rotation by the leakage through an analyser till an eigenmode was reached. No additional improvement of the SHG efficiency could be observed later by further alignment of this angle which was in good agreement with the calculated value from Eq.(30). Note that the dispersion of the optic axis angle V_Z (see Eq.(24) and Fig. 7) is relatively small and the deviation between visible (633 nm) and 2300 nm is less than 2° , so that the error originating from that effect is estimated to be less than 5%. The following results are values of the $\mathbf{d}^{(2)}$ tensor components scaled to $\lambda = 2300$ nm by using Miller's rule, i.e. assuming the same wavelength dispersion for the second-order nonlinearity as for the linear susceptibility,

$$d_{31}(\text{LIS}) = 7.25 (\pm 5\%) \text{ pm/V}, \quad (42)$$

$$d_{24}(\text{LIS}) = 5.66 (\pm 10\%) \text{ pm/V}, \quad (43)$$

$$d_{33}(\text{LIS}) = -16 (\pm 25\%) \text{ pm/V}. \quad (44)$$

The uncertainties are related to the group velocity mismatch and to the relatively large angular acceptance using thin samples. The above results are in very good

agreement with the values obtained in the previous subsection by a completely different strategy and we also confirmed the different sign of the diagonal element d_{33} as established by Boyd *et al* [9]. Note that if the results from Ref. [9] which were obtained by non-phase-matched SHG are renormalized using a more recent value of $d_{14}(\text{GaAs})=83 \text{ pm/V}$ [35] we arrive at $d_{31} = 6.14 \text{ pm/V}$, $d_{32} = 5.31 \text{ pm/V}$ and $d_{33} = 9.8 \text{ pm/V}$. Having in mind the different wavelength (10.6 μm) used in Ref. [9], we obtain a good agreement within $\pm 20\%$ with the present work for all three nonlinear coefficients.

C. Effective nonlinearity of LIS

Once the nonlinear coefficients are determined the effective nonlinearity d_{eff} can be easily calculated in the principal planes using Eqs. (31)-(33). The main conclusion drawn in Ref. [9], namely that the maximum d_{eff} is achieved in the X-Y plane where it is wavelength (angle) independent because of the similar magnitude of d_{24} and d_{15} , remains valid with our updated values for the d_{ij} 's. However, as already mentioned in subsection VII B, interesting effects can be expected for propagation outside the principal planes. Fig. 14 shows the calculated $d_{\text{eff}}(\varphi, \theta)$ for SHG using Eq. (28)-(29) with the nonlinearities obtained in the previous subsection and assuming for simplicity a constant angle $V_Z = 66^\circ$ between the optic axes and the Z-principal axis (see Fig. 7) which for the wavelengths selected leads to only negligible errors. The fundamental wavelengths indicated in the figure correspond exactly to the phase-matching stereographic projections presented in Fig. 9 where the values for the polar angle θ for the limiting cases $\varphi = 0, 90^\circ$ can be seen. As can be seen from the figure for type-I SHG in the Hobden classes 9, 10, and 11 (see subsection VII A and Ref. [62]) the improvement in d_{eff} when propagating outside the principal planes is not significant. On the contrary for Hobden class 13, it is definitely advantageous to use propagation outside the principal planes for maximum d_{eff} in type-I SHG. In type-II SHG the curves in Fig. 14 have a different character and maximum d_{eff} is achieved always in the X-Y plane which is advantageous as compared to type-II SHG in the Y-Z plane.

For various applications it is important to consider the down-conversion into the mid-IR of high power sources, e.g. lasers emitting at 1064 nm (Fig. 15). For the selected wavelengths, the absolute negative extremum of the type-II curves which occurs in X-Y plane (right end, with $d_{\text{eff}}^{\text{oe}}(90^\circ, \varphi) \simeq -6.5 \text{ pm/V}$) is larger than the extremum of the type-I curves in the X-Z plane (i.e. on the left side, with $+4 < d_{\text{eff}}^{\text{oe}}(\theta, 0^\circ) < 5 \text{ pm/V}$). Hence type-II interaction in the X-Y plane has larger d_{eff} than type-I interaction in the X-Z plane. However, propagation outside the principal planes allows to reach a slightly larger maximum $-7 < d_{\text{eff}}^{\text{ssf}}(\theta, \varphi) < -7.5 \text{ pm/V}$ for type-I interaction which can be advantageous since other parameters like e.g. the spectral bandwidth can be better in type-I

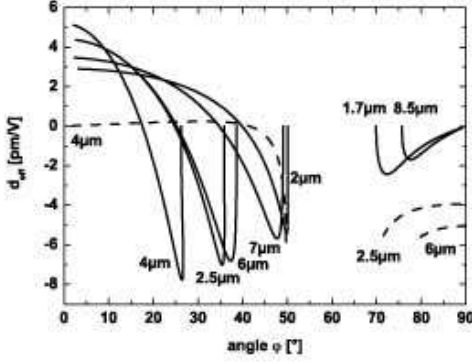


FIG. 14: Effective nonlinearity for type-I (*ssf*, solid lines) and type-II (*fsf*, dashed lines) SHG outside the principal planes of LIS as a function of the azimuthal angle φ . The labels indicate the fundamental wavelengths corresponding to the (φ, θ) phase-matching loci of Fig. 9.

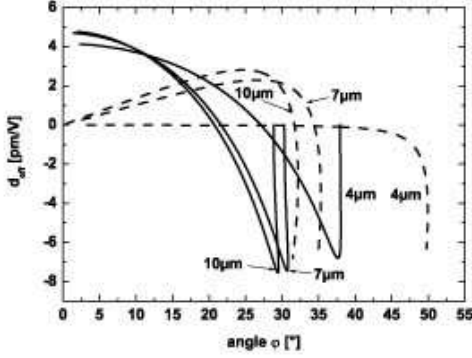


FIG. 15: Effective nonlinearity for type-I (*ssf*, solid lines) and type-II (*fsf*, dashed lines) down-conversion of $\lambda_3 = 1064$ nm radiation (optical parametric generation, amplification or oscillation) to three selected idler wavelengths $\lambda_1 = 4, 7, 10$ μm for propagation outside the principal planes of LIS as a function of the azimuthal angle φ .

interaction. We believe the potential for future applications of LIS in the mid-IR is related also to the utilization of propagation schemes outside the principal planes.

IX. PARAMETRIC DOWN-CONVERSION

A. Femtosecond optical parametric amplification

As outlined in section I LIS possesses the largest bandgap among all known mid-IR nonlinear crystals which results in an extremely low TPA near 800 nm. This unique feature can be utilized for the generation of femtosecond pulses in the mid-IR by down conversion of the most widely used Ti:sapphire femtosecond laser systems

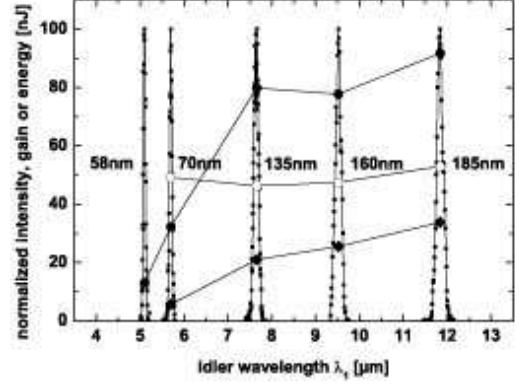


FIG. 16: Idler spectra (the labels indicate FWHM) that demonstrate the achieved tunability with the LIS-based OPA. The black circles show the experimentally achieved output idler energy, the blank circles show the achieved (internal) signal gain, and the diamonds show the applied seed (signal) energy.

operating near 800 nm. In Ref. [21] initial results were presented in the $4.8 - 9$ μm region but the gain and the output energy (2 nJ) were extremely low with a 1.5 mm thick LIS sample used as a seeded OPA. Here we report an improvement by a factor of about 50 for the output idler energy and an extension of the tunability range.

We applied for this experiment a cube of $5 \times 5 \times 5$ mm³ of rose annealed LIS cut at $\varphi = 41^\circ$ and $\theta = 90^\circ$ for type-II interaction in the X-Y plane. The single-stage travelling-wave-type OPA was pumped by longer pulses in order to increase the interaction length. We used 300 fs pump pulses at 820 nm from a Ti:sapphire regenerative amplifier operating at 1 kHz. The pulse lengthening was achieved by adjustment of the pulse compressor and the pump pulses were not bandwidth-limited (appr. three times the Fourier limit). About 30 μJ were used to generate continuum in a 2 mm thick sapphire plate and 5 different interference filters between 875 and 975 nm were used to select portions (of about 10 nm) of the continuum for seeding the OPA at the signal wavelength (Fig. 16). The seed pulse duration was measured by sum-frequency cross-correlation with a small fraction of the pump pulses in a 0.5 mm thick type-I BBO crystal and deconvolution yielded a pulse FWHM of the order of 400 fs (about 3 times above the Fourier limit). The OPA was pumped by 150 μJ and the pump beam parameters corresponded to a peak on-axis pump intensity of 60 GW/cm².

The mid-IR spectra depicted in Fig. 16 were recorded with a 0.5 m monochromator (150 gr/mm grating) and a liquid-N₂-cooled HgCdTe detector. Tunability from 5 up to almost 12 μm (i.e. the mid-IR cutoff wavelength of Fig. 2) could be demonstrated. From 8 to 12 μm an almost constant energy level exceeding 80 nJ could be achieved, despite the stronger absorption. This can be attributed to the lower group velocity mismatch at longer idler wavelengths [21] and also to the increasing seed

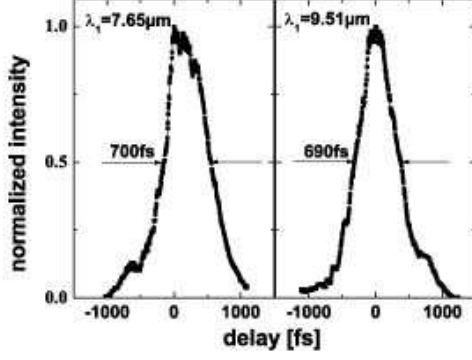


FIG. 17: Cross-correlation traces at two idler wavelengths obtained by sum-frequency mixing with a 820 nm, 300 fs reference pulse. The deconvolved Gaussian pulse durations (FWHM) are in both cases 575 fs.

level which effects compensate for the reduced transmission. The pulse duration of the idler pulses was estimated from sum-frequency cross-correlation with a 820 nm reference pulse in a 0.3 mm thick type-I AGS crystal in which the group mismatch between the two input pulses ranged from 715 fs/mm at $\lambda_1 = 9.5 \mu\text{m}$ to 800 fs/mm at $\lambda_1 = 6.5 \mu\text{m}$. Fig. 17 shows the corresponding cross-correlation traces. The deconvolved pulse duration at 7.65 and 9.51 μm (585 fs in both cases) corresponds to bandwidth-limited Gaussian shaped idler pulses (time bandwidth product equal to 0.44).

Thus LIS is the only nonlinear crystal that permits the direct frequency conversion of short pulses from the 800 nm region to the mid-IR above $\sim 5 \mu\text{m}$ in a *single step* extending the region covered by crystals like LiNbO₃, KNbO₃ or KTP and its isomorphs. The results in this section were obtained with amplified pump pulses at low (kHz) repetition rates. Similar single stage down conversion of high repetition rate (100 MHz) Ti:sapphire femtosecond oscillators should be possible in synchronously pumped LIS-based OPOs.

A further potential application of LIS in femtosecond technology which relies on the extremely low TPA near 800 nm [21] is related to the generation of single (or sub-) cycle femtosecond pulses (both at low and high repetition rates) in the mid-IR by DFG of spectral components belonging to the same broadband spectrum of an ultrashort 800 nm pulse [79]. If 15 fs long bandwidth-limited pulses centered at 800 nm are used for this purpose the generated mid-IR wavelength is about 10 μm at which wavelength a 30 fs long pulse would possess only one optical cycle. The basic limitation in the conversion efficiency when using GaSe as previously demonstrated for this purpose [79] was its strong TPA at 800 nm.

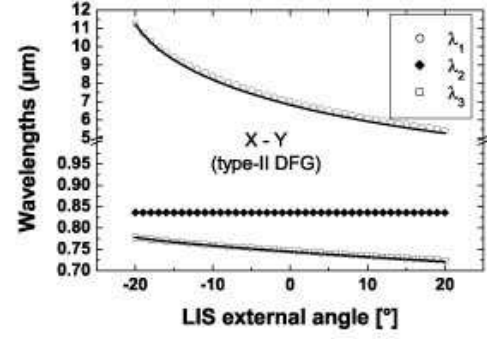


FIG. 18: Wavelength and angle tuning characteristics of type-II (*eoe*) DFG of two cw Ti:Sapphire lasers in LIS. The solid lines are calculated from the Sellmeier equations of Subsection VI A.

B. Continuous-wave mid-IR DFG

We report in this subsection the first DFG experiments ($5.5 < \lambda_1 < 11.3 \mu\text{m}$) ever performed with LIS, whose partial results were already used to derive the accurate Sellmeier equations of Subsection VI A. Continuous-wave (cw) DFG is most suited for high-resolution spectroscopy in the mid-IR range: when both DFG laser sources have linewidths $< 1 \text{ MHz}$ the mid-IR radiation at λ_1 allows to perform sub-Doppler spectroscopy of heavy atmospheric molecules with only $\sim 1 \mu\text{W}$ of power. Until now, cw DFG of two near-IR lasers for the generation of deep mid-IR light either used AGS [80, 81, 82] or GaSe [83]. We demonstrate that LIS is an alternative promising candidate, since we report cw parametric generation up to 11.3 μm with an uncoated yellowish LIS sample of dimension $5 \times 5 \times 10 \text{ mm}^3$ ($L = 10 \text{ mm}$), cut in the X-Y plane for type-II (*eoe*) DFG at ($\theta = 90^\circ, \varphi = 42^\circ$).

Two tunable cw single-frequency Ti:sapphire lasers were used as difference-frequency mixing sources. The laser beams, orthogonally polarized, were collinearly focused onto the crystal with a 35-cm-focal length lens, yielding a nearly optimal $w_0 = 55 \mu\text{m}$ waist for both pump wavelengths $\lambda_3 < \lambda_2$. The pump wavelengths were blocked after the sample by a 1-mm thick uncoated germanium (Ge) filter and the mid-IR radiation was detected by a calibrated liquid-N₂-cooled HgCdTe photoconductive detector with a $1 \times 1 \text{ mm}^2$ active area. The detected voltage was amplified by a low-noise preamplifier and fed to a lock-in amplifier.

In Table IV, we have already seen that at fixed $\varphi = 42^\circ$, wavelength tuning alone can cover only the 6.6 – 7 μm range, limited by the tunability range of the Ti:sapphire lasers (from curves 2-3 of Fig. 13, a tunability range extending into the blue would be required to extend the DFG to $\sim 10 \mu\text{m}$). Taking profit of angle tuning, mid-IR radiation was generated with broad wavelength tunability in the 5.5 – 11.3 μm spectral region with combined pump laser wavelength (λ_3) and crystal angle (φ)

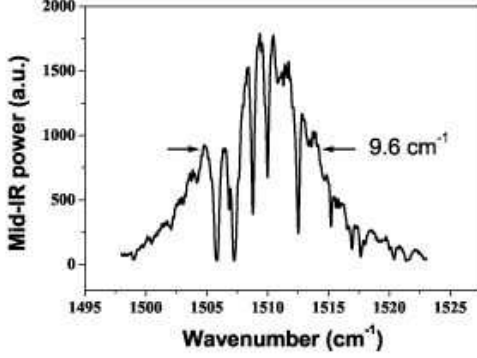


FIG. 19: Mid-IR DFG spectral tuning curve in pump tuning mode around $\lambda_3 \simeq 765$ nm. The other wavelength was fixed at $\lambda_2 = 865.3$ nm. In this frequency scan, we could observe atmospheric water vapor absorption lines in laboratory ambient air over 42.5-cm open path between the LIS crystal and the HgCdTe detector.

tuning [81]: in Fig. 18 one Ti:sapphire laser was fixed at $\lambda_2 \sim 836$ nm, and the other (λ_3) was tuned from 724 to 778 nm. The solid lines are calculated phase-matching curves from Eqs.(21)-(23), highlighting the accuracy of the Sellmeier equations that were fitted using the fixed-angle DFG data of Table IV.

Fig. 19 displays the mid-IR spectral tuning bandwidth around 1510 cm^{-1} ($\lambda_1 \sim 6.6 \mu\text{m}$), when λ_2 is set at 865.3 nm and λ_3 is tuned around 765 nm, corresponding to a quasi-normal incidence phase-matching. A $\Delta\bar{\nu}_1 \sim 10 \text{ cm}^{-1}$ ($\bar{\nu} = 1/\lambda \equiv \nu/c$) FWHM spectral bandwidth is obtained, within which sharp atmospheric water vapor absorption lines can be observed. The FWHM plane-wave spectral acceptance for this pump tuning mode expresses as [3]

$$\Delta\nu_1 = 1.722 \frac{\pi}{L} \left[\frac{\partial \Delta k}{\partial \nu_1} \right]_{\nu_1^{\text{PM}}}^{-1} \quad (45)$$

where $\partial \Delta k / \partial \nu_1$ can be expanded, taking the constraint $\nu_3 - \nu_2 = \nu_1$ into account, as

$$\begin{aligned} \frac{\partial \Delta k}{\partial \nu_1} &= \frac{2\pi}{c} \left[n_3(\varphi) - \lambda_3 \frac{\partial n_3(\varphi)}{\partial \lambda_3} - n_1(\varphi) + \lambda_1 \frac{\partial n_1(\varphi)}{\partial \lambda_1} \right] \\ &\equiv 2\pi \Delta_{31}. \end{aligned} \quad (46)$$

In Eq.(46), the angle-dependent indices are the extraordinary indices in the X-Y plane. From (45)-(46), the calculated spectral acceptance is $\Delta\nu_1 = 214 \text{ GHz}$ ($\Delta\bar{\nu}_1 \simeq 7.2 \text{ cm}^{-1}$) corresponding to a pump tuning over $\Delta\lambda_3 = 0.42 \text{ nm}$. The bandwidth broadening observed in Fig. 19 is attributed to the focused beam effect [84].

Let us note that despite the strong mid-IR absorption at $11.3 \mu\text{m}$ (Fig. 2), we could still detect $\sim 3 \text{ nW}$ mid-IR power for input powers $P_3 = 200 \text{ mW}$ and $P_2 = 265 \text{ mW}$.

This power is generated by the last exit layers of material. For the same incident powers, the detected power at $\lambda_1 = 7 \mu\text{m}$ was $P_1 = 33.5 \text{ nW}$. The net conversion efficiency at this wavelength, corrected for all Fresnel optical loss, amounted to $\Gamma = P_1/P_3P_2 \simeq 1.6 \mu\text{W/W}^2$. Using the general focused-beam theory for DFG [84] that evaluates the focusing function h for type-II DFG for the given focusing parameters, walk-off value ($|\rho_{1,3}| = 0.97^\circ$) and absorption loss ($\alpha_3 \sim 0.15 \text{ cm}^{-1}$, $\alpha_2 \sim 0.1 \text{ cm}^{-1}$, $\alpha_1 \sim 0.05 \text{ cm}^{-1}$), we derive an effective nonlinear coefficient $d_{\text{eff}}(7 \mu\text{m}) \simeq 5.3 \text{ pm/V}$. This value is slightly lower than the calculated value using Eq.(31) and the determined values of d_{24} and d_{15} (Eqs.(43)-(42)), $d_{\text{eff}} \simeq 6.55 \text{ pm/V}$. The difference may arise from the residual atmospheric water absorption lines in this region.

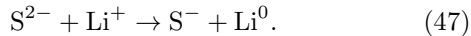
X. LASER-INDUCED DAMAGE IN LiInS₂

Illumination with various laser sources resulted in the following photo-induced phenomena observed in LIS, whose magnitude depends on wavelength and pulse duration: (i) micro-cracking (at $\lambda = 5 \mu\text{m}$ using femtosecond pulses from a free-electron laser [20]); (ii) dendrite structure formation (at $\lambda = 1.079 \mu\text{m}$ using nanosecond pulses); (iii) photo-induced absorption (PIA) as grey-tracks (at $\lambda = 0.8 \mu\text{m}$ using femtosecond pulses). Optical damage of (i) and (ii) kinds is irreversible, while PIA damage is to a certain extent reversible. It disappears at lower levels spontaneously after several hours of storage at room temperature or several minutes of illumination with $\lambda > 500 \text{ nm}$. The PIA was detected first in femtosecond OPA experiments with a 1.5mm thick LIS sample pumped by a 1kHz Ti:sapphire regenerative amplifier delivering pulses at 800nm with a duration of 200fs and energy of $200 \mu\text{J}$ [21]. No surface damage was observed in these experiments up to a peak on-axis intensity of 140 GW/cm^2 . In principle as with other materials optical damage in the femtosecond regime is expected to occur indirectly as a result of filamentation and self-focussing through higher-order nonlinear effects. These studies permitted to estimate only an upper limit on the nonlinear absorption losses at 800 nm which were independent of polarization and presumably caused by inclusions. They could not be fitted by a TPA process and the estimated upper limit of TPA is $\beta_{\text{TPA}} \sim 0.04 \text{ cm/GW}$ at 800 nm [21]. This is about 100 times lower than the $\beta_{\text{TPA}} = 3.5 - 5.6 \text{ cm/GW}$ (depending on the polarization) fitted for a 0.3mm thick AGS crystal under identical conditions, which is a manifestation of the advantages of LIS related to its larger bandgap. An updated value for the upper TPA limit that we derived for a different sample, namely the LIS crystal used in Subsection IX A, is only slightly higher: $\beta_{\text{TPA}} = 0.05 \text{ cm/GW}$. Note that recent TPA measurements on KNbO_3 (which belongs to the same class mm²) at 846 nm using a 5-mm thick sample phase-matched for cw blue light generation yielded a TPA magnitude ($\beta_{\text{TPA}} = 3.2 \text{ cm/GW}$) of the same order

as that for AGS [85]. In the experiment of Ref. [21] the gray tracks formation (leading to PIA) was attributed to non-phase-matched SHG and residual blue light absorption, i.e. this damage mechanism is only indirectly related to the high intensity of the femtosecond pulses that resulted in higher probability for unwanted SHG. Subsequently differential absorption (before and after illumination) was measured that had a magnitude reaching several cm^{-1} and extended from 400 nm up to the near-IR ($1 - 2 \mu\text{m}$) [86]. Well pronounced maxima of this absorption were observed at 430 nm and 650 nm. This photochromic induced-absorption is similar to the so-called Blue-Induced Infrared Absorption (BLIIRA) observed in SHG experiments with KNbO_3 , for which an increased near-IR absorption coefficient (0.011 to 0.056 cm^{-1} depending on the sample and corresponding to 2.5 to 9 times the usual linear absorption) at the fundamental wavelength of 860 nm was detected with 100 mW of blue SH power (30 kW/cm^2) generated with a Ti:sapphire laser [87]. The BLIIRA damage was also reported to be reversible, after a few hours of relaxation at room temperature, and could be minimized by heating the crystal or pumping at longer wavelengths [88].

In order to understand the origin of the PIA in LIS, we proceeded with a direct illumination of LIS samples at $300 < \lambda < 450 \text{ nm}$ using a 1 kW Xe lamp filtered through a monochromator for ~ 10 minutes: The same coloration effect was indeed obtained, with a maximum effect at 360 nm excitation and vanishing at wavelengths shorter than 300 nm. Thus the PIA observed in the OPA experiments is really caused by linear absorption of non-phase matched blue SHG by point defects present in the lattice. In line with the photo-induced signal in absorption spectra (see Fig.3 in Ref. [86]), a complicated system of lines appears in the Electron Spin Resonance (ESR) spectrum. Analysis of the angular dependence allowed us to reveal the superposition of two spectra related to different paramagnetic defects. One of them has a spin $S = 1/2$ and an anisotropic g -factor with the following principal values of the \mathbf{g} -tensor: $g_1 = 2.160$, $g_2 = 2.023$, $g_3 = 2.023$. This spectrum is associated with a center of axial symmetry with g_1 , directed along the In-S bond and is related to sulfur S^- ion in a regular site. The second spectrum comprising a broad line at $H \sim 3300 \text{ Gauss}$ ($g = 2.0024$) is associated with Li^0 .

The interpretation of these results is the following. At short-wavelength excitation ($\lambda < 450 \text{ nm}$) the following recharge process occurs in LIS:



Such excitation produces free charge carriers which are captured in some deep traps and can be released at $\lambda > 500 \text{ nm}$ illumination. We established that the gray track formation is maximized for excitation near 360 nm but dropped by one order of magnitude at 420 nm, which means that in OPO/OPA experiments it can be reduced by using slightly longer pump wavelength λ_3 . Note that the same process also takes place at x-ray irradiation,

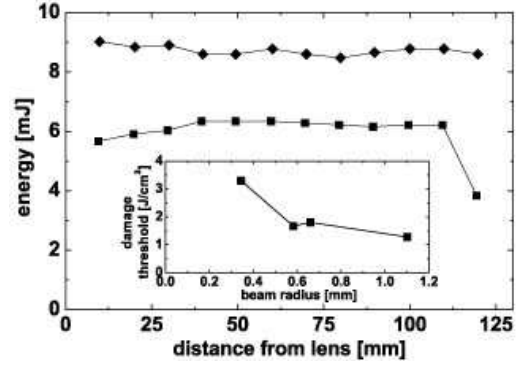


FIG. 20: Measured pulse energy with crystal inserted (squares) and without it (diamonds). The drop in transmitted energy (last square) indicates damage formation. Inset: Damage threshold, expressed as fluence, versus beam radius at the crystal surface.

which is used for crystal orientation when fabricating optical elements: some darkening occurs sometimes in the bulk sample during this operation. The PIA magnitude was found to be dependent on the LIS composition [89]: The effect is minimum in the case of nearly stoichiometric composition. The PIA was also found to be much more pronounced in LIS than in LISe.

Systematic optical damage threshold measurements were performed with Nd:YAG lasers at 1064 nm - i.e. well within the clear transmission range and far from the TPA region. Initial measurements with a 6 W cw focused Nd:YAG laser beam failed to produce measurable damage, and subsequent measurements were performed with a pulsed laser. The pulse energy was varied between 6 mJ and 25 mJ at a repetition rate of 10 Hz and a pulse width of about 10 ns. The collimated Gaussian beam with a beam radius of $w_{in} = 1.47 \text{ mm}$ was focused with a 200 mm focal length lens to produce a beam waist with a radius of $w_0 = 46 \mu\text{m}$. The crystal used was a rose sample with dimensions $4 \times 5 \times 5 \text{ mm}^3$ ($\theta = 90^\circ$, $\varphi = 24^\circ$). The corresponding fluences ranged from 0.19 J/cm^2 to 752 J/cm^2 , and by using different pulse energies, the same fluence could be sustained over a range of spot radii. The Gaussian character of the beam was verified, and the beam radius measured by the knife-edge technique. The onset of radiation damage was determined from the observed sudden drop in the transmitted signal as shown in Fig. 20. At each experimental point, the crystal was inspected visually in a low-power microscope, and the drop in transmission was found to correlate with the onset of visible damage at the surface. By performing experiments with different pulse energies it was found that the damage threshold, expressed in J/cm^2 , tends to decrease with increasing spot size as seen in the inset figure of Fig. 20. Although the amount of data is too limited to warrant a detailed analysis, it suggests a levelling off at about 1 J/cm^2 at large spot sizes (i.e. a peak intensity threshold of 100 MW/cm^2), and this value agrees

well with the value 1.1 J/cm^2 reported by Knippels *et al.* at a wavelength of $5 \mu\text{m}$ [20]. The observed dependence in the inset figure is understandable in view of the fact that as the spot size increases, it becomes increasingly difficult for heat generated at the centre to diffuse to the unexposed regions of the crystal. In Fig. 20, the initial increase of transmitted energy reflects the fact that the center of the beam is too close to the edge to allow the entire beam to be intercepted by the crystal when the beam radius is largest. In some cases damage was found to extend into the interior of the crystal.

These damage properties should be discussed in comparison with available damage data on AGS or AGSe. For AGS under cw pumping the onset of thermal lensing has been previously evaluated at $\sim 11 \text{ kW/cm}^2$ from a cw AGS doubly resonant OPO containing $\sim 3 \text{ W}$ of circulating power at 1.26 and $2.52 \mu\text{m}$ focused to a waist of $w_0 = 90 \mu\text{m}$ [6, 7]. The cw damage threshold value is actually unknown, but is estimated to occur in the range $\sim 20 - 40 \text{ kW/cm}^2$ [90], despite a report that 3.5 W of cw Nd:YAG radiation focused to a waist of $20 \mu\text{m}$ (280 kW/cm^2) did not damage an AGS sample [91]. For AGSe, the measured damage threshold at $9 \mu\text{m}$ (cw CO_2 laser) was ascertained to be $5 - 22 \text{ kW/cm}^2$ [92], corroborating that chalcopyrites display extremely low cw damage threshold. The fact that for 6 W at 1064 nm , focused down to $w_0 = 40 \mu\text{m}$ no visible damage was observed in the LIS sample sets the cw damage threshold to a lower limit of $> 120 \text{ kW/cm}^2$. The 5 times larger thermal conductivity of LIS as compared to AGS certainly favors the use of LIS in intra-cavity cw applications. Under similar nanosecond pulsed regime, however, the $\sim 1 \text{ J/cm}^2$ damage threshold measured with LIS is comparable to the threshold found for AGS or AGSe [93, 94]. Independent measurements at longer wavelengths ($9.55 \mu\text{m}$) with 30 ns long pulses yielded, under identical experimental conditions, damage thresholds of 6.5 J/cm^2 for LIS [57] and 5.5 J/cm^2 and 4.2 J/cm^2 for AGS and AGSe, respectively [95].

From these preliminary damage threshold investigations, it is premature to assess whether the damage mechanisms are due to native point defects or are intrinsic to the compound. Considering the current state-of-the-art of residual absorption on this compound, one may expect that with an improvement in residual transparency and a better control of the growth parameters toward the production of stoichiometric material, the above damage threshold values can be improved.

XI. CONCLUSIONS

We have characterized the main physical properties of the newly emerging lithium thioindate chalcogenide semiconductor that are relevant for nonlinear applications from the visible up to the deep mid-IR. Table VI summarizes these properties, as well as those determined in previous works. LiInS_2 or LIS can now be consid-

ered as a mature compound and its future widespread use in nonlinear devices should refine all the data collected from this investigation campaign. Among its most relevant advantages over the existing mid-IR crystals, one may quote its excellent thermal stability and high damage threshold suitable for high power laser applications and its extremely extended phase-matching capabilities (over its whole transparency range) using either type-I or type-II interactions in or out-of principal planes. Such an extended phase-matching capability is still compatible with low birefringence walk-off angles. LIS is the only existing material for direct down-conversion from the near-IR to the deep mid-IR up to $12 \mu\text{m}$, owing to its highest bandgap energy. Its effective nonlinearity of $\sim 7 \text{ pm/V}$ (slightly lower than that of the chalcopyrite crystals) is substantially higher than that of the oxides of the KTP family and is almost constant for type-II interaction in the azimuthal principal plane. We have shown that LIS should be very promising for the frequency down-conversion of femtosecond laser sources. At equivalent loss level, LIS would be less subject to thermal lensing than AGS [6, 7] permitting its use in cw OPOs for deep mid-IR generation.

The next challenge and effort will be directed to the detailed studies on its eventual ferro-electric properties. In contrast with the chalcopyrites, LIS and LISe are pyroelectric as the orthorhombic symmetry oxides (KTP isotopes) belonging to the same $mm2$ point group. The spontaneous polarization is due to the fact that in each bipyramid formed by two adjacent tetrapores (Fig. 1) only one is occupied by a Li^+ cation. The other one is empty, which corresponds to a negative effective charge. An intriguing issue, which has not still received a definite answer, is whether such Li-chalcogenides can be related to ferroelectric materials, i.e. if it is possible to invert their spontaneous polarization along the polar c -axis. In their short note [52], Negran *et al* concluded that LIS and LISe do not display a para-to-ferroelectric phase transition from the absence of a sudden anomalous rise in the record of the pyro-electric current versus temperature. This is not surprising because of the screening effect of the high ionic conductivity of Li. They measured a pyroelectric coefficient $p^r(300\text{K}) = 2.6 \times 10^{-10} \text{ C}/(\text{cm}^2 \cdot \text{K})$. A more recent and reliable measurement of the pyro-electric coefficient performed with our rose samples yielded a 2.3 times higher value (Table VI), which is 5 times smaller than the value for KTP [96]. In contrast with Negran *et al*'s report, a strong increase of the pyro-current slightly above room-temperature, preceded by a sharp current spike, was noticed but this increase was attributed to space charge relaxation of the thermally-activated Li^+ cations [55].

The issue about whether Li-chalcogenides are (or are not) related to ferroelectrics is of upmost importance, considering their deep mid-IR transparency which would allow to fabricate quasi-phase matched periodically-poled structures for wavelengths longer than $\sim 4 - 5 \mu\text{m}$, which is the current limitation of oxide-based ferroelectrics such

TABLE VI: Summary of the main physical properties of LiInS₂.

CRYSTALLOGRAPHIC DATA	
Structure	Wurtzite-type (β -NaFeO ₃ structure)
Symmetry, point group	Orthorhombic, mm2 (negative biaxial)
Space group	Pna2 ₁
Lattice parameters (Å)	$a = 6.874$; $b = 8.033$; $c = 6.462$ (Ref. [18])
Principal axes assignment	$(X, Y, Z) \longleftrightarrow (b, a, c)$
Density (g/cm ³)	3.46
Microhardness (Pa)	145×10^7 (Refs. [26, 27])
OPTICAL PROPERTIES	
Optical transmission (μm)	0.34 - 11.5
Bandgap energy ($T = 300$ K) (eV)	3.55 ($E \parallel c$); 3.61 ($E \parallel b$); 3.58 ($E \parallel a$) (Ref. [18])
Indices of refraction at $T = 20^\circ$:	
$\lambda = 0.532 \mu\text{m}$	$n_X = 2.2413$; $n_Y = 2.2824$; $n_Z = 2.2991$
$\lambda = 1.064 \mu\text{m}$	$n_X = 2.1288$; $n_Y = 2.1645$; $n_Z = 2.1734$
$\lambda = 10.6 \mu\text{m}$	$n_X = 2.0200$; $n_Y = 2.0566$; $n_Z = 2.0595$
Optical axis angles ($0.35 \mu\text{m} < \lambda < 11.5 \mu\text{m}$)	$55^\circ < V_Z < 80^\circ$
Birefringence walk-off at 1064 nm (mrad)	$\rho_{X-Y} = 14.7$; $\rho_{X-Z} = 20$
SHG fundamental wavelength range (nm)	1617 - 8710
Thermo-optic coefficients ($10^{-5}/^\circ\text{C}$)	
at 1064 nm, $T = 20^\circ\text{C}$	$dn_X/dT = 3.72$; $dn_Y/dT = 4.55$; $dn_Z/dT = 4.47$
Absorption coefficient at 1.064 μm (cm ⁻¹)	$\alpha \leq 0.04$
Laser damage threshold:	
• surface, at 10 ns, $f = 10$ Hz, $\lambda = 1.064 \mu\text{m}$	1 J/cm ²
• bulk, at 500 fs, $f = 25$ MHz, $\lambda = 1.064 \mu\text{m}$	> 6 GW/cm ² (Ref. [20])
• surface, at 200 fs, $f = 1$ kHz, $\lambda = 0.8 \mu\text{m}$	> 140 GW/cm ² (Ref. [21])
Two-photon absorption at 0.8 μm (cm/GW)	$\beta_{\text{TPA}} \leq 0.05$
Nonlinear optical coefficients (pm/V)	
• by cw SHG at 2.5 μm	$d_{15} = 7.9(\pm 1.6)$; $d_{24} = 5.7(\pm 1.2)$
• by femtosecond SHG at 2.3 μm	$d_{31} = 7.2(\pm 0.4)$; $d_{24} = 5.7(\pm 0.6)$; $d_{33} = -16(\pm 4)$
THERMAL PROPERTIES	
Melting point ($^\circ\text{C}$)	$T_{\text{melt}} \sim 1000$
Thermal expansion at $T = 20^\circ\text{C}$ ($10^{-5}/^\circ\text{C}$)	$\alpha_X = +1.64$; $\alpha_Y = +0.91$; $\alpha_Z = +0.68$
Specific heat at $T = 300$ K (J/mol/K)	$C_p = 92.9$
Thermal conductivity at $T = 300$ K (W/m/ $^\circ\text{C}$)	$K_X = 6.2$; $K_Y = 6.0$; $K_Z = 7.6$ (Ref. [50])
ELECTRICAL PROPERTIES	
Pyroelectric coefficient at $T = 300$ K ($\mu\text{C}/\text{m}^2\text{K}$)	6 (Ref. [55])
Pure electro-optic coefficients (pm/V)	$r_{13} = 1.0$; $r_{23} = 0.4$; $r_{33} = -1.3$
Piezo-electric coefficients (pm/V)	$d_{31} = -5.6$; $d_{32} = -2.7$; $d_{33} = +7.5$
Electric conductivity ($\Omega^{-1}\text{cm}^{-1}$)	$\sigma_Z = 4.3 \times 10^{-10}$ (Ref. [98]); $\sigma = 1 \times 10^{-12}$ (Refs. [22, 27])

as LiNbO₃ or KTiOPO₃. The measurement of the Curie temperature (a temperature at which the material tends to loose its spontaneous polarization), the study of its dielectric conductivity versus an applied ac electric field in order to reveal a dielectric hysteresis loop (and the value of the coercive field) have to be performed to answer to the question.

Finally, we started to investigate other Li-containing compounds such as LiInSe₂ (LISE), LiGaS₂ (LGS), LiGaSe₂ (LGSe), LiGaTe₂ (LGT_e) [25, 97].

Acknowledgments

This Concerted Action could not have been possible without the grant awarded by the European Commission (DG12-MZCN directorate), in the frame of its International CO-operation program of the 4th Framework Program (INCO-Copernicus contract No IC15-CT98-0814). The authors are highly grateful

to J.F. Bardeau (Laboratoire de Physique de l'Etat Condensé, Le Mans, France) and to P. Simon and his collaborators (Centre de Recherche sur les Matériaux à Haute Température, Orléans, France) for their expert collaboration in the Raman and IR studies. We also acknowledge V. Drebuschak (Novosibirsk State University, Russia) for the measurement of the specific heat, V. Nadolnny (Institute of Inorganic Chemistry, SB RAS, Novosibirsk) for the Electron Spin Resonance results and J.M. Weulersse, M. Gilbert and G. Mennerat (Commissariat à l'Energie Atomique, Saclay, France) for the use of their nanosecond LiNbO₃-based OPO.

- [1] G.C. Bhar, R.C. Smith, *Optical properties of II-IV-V₂ and I-III-VI₂ crystals with particular reference to transmission limits*, Phys. Stat. Sol. A **13**, 157-168 (1972).
- [2] J.L. Shay, B. Tell, L.M. Schiavone, H.M. Kasper and F. Thiel, *Energy bands of AgInS₂ in the chalcopyrite and orthorhombic structures*, Phys. Rev. B **9**, 1719-1723 (1974).
- [3] V.G. Dmitriev, G.G. Gurzadyan and D.N. Nikogosyan, *Handbook of Nonlinear Optical Crystals*, 3rd revised edn, Springer, Berlin, 1999.
- [4] K. Stoll, J.-J. Zondy and O. Acef, *Fourth-harmonic generation of a continuous-wave CO₂ laser by use of an AgGaSe₂/ZnGeP₂ doubly resonant device*, Opt. Lett. **22**, 1302-1304 (1997).
- [5] D. Lee, T. Kaing and J.-J. Zondy, *An all-diode-laser-based, dual-cavity AgGaS₂ cw difference-frequency source for the 9–11 μm range*, Appl. Phys. B **67**, 363-367 (1998).
- [6] A. Douillet and J.-J. Zondy, *Low-threshold, self-frequency-stabilized AgGaS₂ continuous-wave subharmonic optical parametric oscillator*, Opt. Lett. **23**, 1259-1261 (1998).
- [7] A. Douillet, J.-J. Zondy, A. Yelisseyev, S. Lobanov and L. Isaenko, *Stability and frequency tuning of thermally loaded continuous-wave AgGaS₂ optical parametric oscillators*, J. Opt. Soc. Am. B **16**, 1481-1498 (1999).
- [8] R. Hoppe, *Ternäre Oxide der Alkalimetalle*, Bull. Soc. Chim. France **1965**, 1115-1121 (1965).
- [9] G. D. Boyd, H. M. Kasper, and J. H. McFee, *Linear and nonlinear optical properties of LiInS₂*, J. Appl. Phys. **44**, 2809-2812 (1973).
- [10] T. Kamijoh, K. Kuriyama, *Single crystal growth of LiInS₂*, J. Cryst. Growth **46**, 801-803 (1979).
- [11] T. Kamijoh, K. Kuriyama, *Blue-band emission in LiInS₂ crystals*, J. Appl. Phys. **51**, 1827-1828 (1981).
- [12] T. Kamijoh, T. Nozaki, K. Kuriyama, *A photoluminescence study of lithium ternary compounds*, Nuovo Cimento **2D**, ser.1, 2029-2033 (1983).
- [13] K. Kuriyama, T. Kato, A. Takahashi, *Optical band gap and blue-band emission of a LiInS₂ single crystal*, Phys. Rev. B **46**, 15518-15519 (1992).
- [14] K. Kuriyama, T. Kato, A. Takahashi, *Blue-band emission of LiInS₂ single crystals grown by the indium solution method*, Jpn. J. Appl. Phys. **32**, suppl. 32-3, 615-617 (1993).
- [15] K. Kuriyama and T. Kato, *Optical band gap and photoluminescence studies in blue-band region of Zn-doped LiInS₂ single crystals*, Solid State Commun. **89**, 959-962 (1994).
- [16] M.I. Golovei, E.Yu. Peresh, E.E. Semrad, *Production and characteristics of semiconductor materials of complex composition, promising for quantum electronics and opto-electronics*, Kvantovaya Elektronika, Kiev, no. **20**, 93-103 (1981).
- [17] K. Kuriyama, J. Saitoh, *Preparation and optical properties of LiInS₂ thin films*, Thin Solid Films **111**, 331-337 (1984).
- [18] L. Isaenko, I. Vasilyeva, A. Yelisseyev, S. Lobanov, Y. Malakhov, L. Dovlitova, J.-J. Zondy and I. Kavun, *Growth and characterization of LiInS₂ single crystals*, J. Cryst. Growth **218**, 313-322 (2000).
- [19] A. Yelisseyev, L. Isaenko, S. Lobanov, J.-J. Zondy, A. Douillet, I. Thénot, Ph. Kupecek, G. Mennerat, J. Man-
gin, S. Fossier and S. Salaiin, *New ternary sulfide for double applications in laser schemes*, in Advanced Solid State Lasers, H. Injeyan, U. Keller, and C. Marshall, eds., OSA-TOPS Vol. **34**, 561-568 (Optical Society of America, Washington D.C., 2000).
- [20] G. M. Knippels, A. P. G. van der Meer, A. M. MacLeod, A. Yelisseyev, L. Isaenko, S. Lobanov, I. Thénot and J.-J. Zondy, *Mid-infrared (2.75-6.0 μm) second-harmonic generation in LiInS₂*, Opt. Lett. **26**, 617-619 (2001).
- [21] F. Rotermund, V. Petrov, F. Noack, L. Isaenko, A. Yelisseyev, S. Lobanov, *Optical parametric generation of femtosecond pulses up to 9 μm with LiInS₂ pumped at 800 nm*, Appl. Phys. Lett. **78**, 2623-2625 (2001).
- [22] J. Brückner, V. Krämer, E. Nowak, V. Riede, B. Schumann, *Crystal growth and characterization of LiInS₂*, Cryst. Res. Technol. **31**(Supplement), 15-18 (1996).
- [23] A. Eifler, V. Riede, J. Brückner, S. Weise, V. Krämer, G. Lippold, W. Schmitz, K. Bente and W. Grill, *Band gap energies and lattice vibrations of the lithium ternary compounds LiInSe₂, LiInS₂, LiGaSe₂ and LiGaS₂*, Jpn. J. Appl. Phys. **39**, suppl.39-1, 279-281(2000).
- [24] S. Pearl, S. Fastig, Y. Ehrlich, and R. Lavi, *Limited efficiency of a silver selenogallate optical parametric oscillator caused by two-photon absorption*, Appl. Opt. **40**, 2490-2492 (2001).
- [25] L. Isaenko, A. Yelisseyev, S. Lobanov, V. Petrov, F. Rotermund, G. Sleky, and J.-J. Zondy, *LiInSe₂: A biaxial ternary chalcogenide crystal for nonlinear optical applications in the mid-infrared*, J. Appl. Phys. **91**, 9475-9480 (2002).
- [26] S.K. Kovach, E.E. Semrad, Yu.V. Voroshilov, V.S. Gerasimenko, V.Yu. Slivka, and N.P. Stasyuk, *Preparation and principal physicochemical properties of alkali metal indates and thioindates*, Inorganic Mat. **14**, 1693-1697 (1978) [transl. from Isv. Akad. Nauk SSSR, Neorg. Materialy **14**, 2172-2176 (1978)].
- [27] Z.Z. Kish, V.B. Lazarev, E.E. Semrad, H. Yu. Peresh, and I.V. Galagovets, *Some properties of single crystals of LiInS₂ and NaInS₂*, Inorganic Mat. **20**, 647-649 (1984) [transl. from Izv. Akad. Nauk SSSR, Neorg. Materialy **20**, 750-752 (1984)].
- [28] J. Brückner, *I-III-VI Verbindungshalbleiter mit Lithium als Gruppe I-Element: Kristallzüchtung und Charakterisierung*, Ph. D dissertation thesis, Albert-Ludwigs Univ., Freiburg, Germany (1997).
- [29] L. Isaenko, A. Yelisseyev, J.-J. Zondy, G. Knippels, I. Thénot and S. Lobanov, *Growth and characterization of single crystals of ternary chalcogenides for laser applications*, Opto-Electron. Rev. **9**, 135-141 (2000).
- [30] L. Isaenko, A. Yelisseyev, J.-J. Zondy, G. Knippels, I. Thénot and S. Lobanov, *Growth and characterization of single crystals of ternary chalcogenides for laser applications*, Proc. SPIE **4412**, 342-350 (2001).
- [31] Z.Z. Kish, E.Yu. Peresh, V.B. Lazarev, and E.E. Semrad, *Systematics and the rules of variations in the properties of A^IB^{III}C₂^{VI}-type compounds*, Inorganic Mat. **23**, 697-703 (1987) [transl. from Izv. Akad. Nauk SSSR, Neorg. Materialy **23**, 777-784 (1987)].
- [32] R. S. Feigelson and R. K. Route, *Recent developments in the growth of chalcopyrite crystals for nonlinear infrared applications*, Opt. Eng. **26**, 113-119 (1987).

- [33] A. Yelisseyev, S. Lobanov, L. Isaenko and J.-J. Zondy, *Spectroscopic study of Neodimium-doped LiInS₂ single crystals*, Proc. SPIE **3749**, 687-688 (1999).
- [34] Z.Z. Kish, A.S. Kanishcheva, Yu. N. Mikhailov, V.B. Lazarev, E.E. Sempad, and E. Yu. Peresh, *Synthesis and crystal structure of lithium thioindate LiInS₂*, Soviet Physics /Doklady (Physical Chemistry) **30**, 36-38 (1985) [transl. from Doklady Akad. Nauk SSSR **280**, 398-401 (1985)].
- [35] D.A. Roberts, *Simplified characterization of uniaxial and biaxial nonlinear optical crystals: a plea for standardization of nomenclature and conventions*, IEEE J. Quantum Electron. **28**, 2057-2074 (1992).
- [36] An American National Standard, IEEE Standard on Piezoelectricity, ANSI/IEEE Std 176-1987, IEEE, New York, 1988. Note: This Standard uses Z for the polar axis, X to designate the shorter of the two non-polar unit cell axes, and Y to complete a right-handed coordinate system.
- [37] G. Kühn, E. Piel, H. Neumann, and E. Nowak, *Heat capacity of LiInS₂, LiInSe₂ and LiInTe₂ between 300 and 550K*, Cryst. Res. Technol. **22**, 265-269 (1987).
- [38] H. Sobotta, H. Neumann, V. Riede and G. Kühn, *Lattice vibrations and interatomic forces in LiInS₂*, Cryst. Res. Technol. **21**, 1367-1371 (1986).
- [39] H. Neumann, G. Kühn and W. Möller, *High-temperature specific heat of AgInS₂ and AgGaSe₂*, Cryst. Res. Technol. **20**, 1225-1229 (1985).
- [40] J. Mangin, P. Strimer and L. Lahlou-Kassi, *An interferometric dilatometer for the determination of thermo-optic coefficients of NLO materials*, Meas. Sci. Technol. **4**, 826-834 (1993).
- [41] P. Korczak and C.B. Staff, *Liquid encapsulated Czochralski growth of silver thiogallate*, J. Cryst. Growth **24/25**, 386-389 (1974).
- [42] G.W. Iseler, *Thermal expansion and seed Bridgman growth of AgGaSe₂*, J. Cryst. Growth **41**, 146-150 (1977).
- [43] J.-J. Zondy, and D. Touahri, *Updated thermo-optic coefficients of AgGaS₂ from temperature-tuned noncritical $3\omega - \omega \rightarrow 2\omega$ infrared parametric amplification*, J. Opt. Soc. Am. B **14**, 1331-1338 (1997).
- [44] J. Mangin, S. Salaün, S. Fossier, P. Strimer, J.-J. Zondy, L. Isaenko and A. Yelisseyev, *Optical properties of lithium thioindate*, in "Growth, Fabrication, Devices, and Applications of Laser and Nonlinear Materials", J.W. Pierce, K.I. Schaffers, eds., Proc. SPIE **4268**, 49-57 (2001).
- [45] T.C. Damen, S.P.S. Porto and B. Tell, *Raman effect in zinc oxide*, Phys. Rev. **142**, 570-574 (1966).
- [46] S. Salaün, A. Bulou, J.Y. Gesland and P. Simon, *Lattice dynamics of the fluoride scheelite CaZnF₄*, J. Phys: Cond. Matter **12**, 7395-7408 (2000).
- [47] V.S. D'Ordya, V.A. Stefanovich, E.I. Pan'ko, V.B. Lazarev, E. Yu. Peresh and Z.Z. Kish, *Raman scattering in LiInS₂*, Inorganic Mat. **24**, 461-464 (1988) [transl. from Izv. Akad. Nauk SSSR, Neorg. Materialy **24**, 555-559 (1988)].
- [48] H. Neumann, *Vibrational properties of LiGaO₂. II: Theoretical model considerations*, Cryst. Res. Technol. **21**, 1361-1366 (1986).
- [49] H. Neumann, *Lattice vibrations in A^IB^{III}C^{VI} chalcopyrite compounds*, Helv. Phys. Acta **58**, 337-346 (1985).
- [50] C. Ebberts, Lawrence Livermore National Laboratory, USA, private communication.
- [51] S. Fossier, *Métrologie des propriétés optiques de cristaux massifs; Etude de LiInS₂, matériau optiquement non linéaire pour l'infrarouge moyen*, Thèse de Doctorat, Université de Bourgogne, France (2002).
- [52] T.J. Negran, H.M. Kasper and A.M. Glass, *Pyroelectric and electrooptic effects in LiInS₂ and LiInSe₂*, Mat. Res. Bull. **8**, 743-748 (1973).
- [53] C.G.B. Garrett, *Nonlinear optics, anharmonic oscillators and pyroelectricity*, IEEE J. Quantum Electron. **QE-4**, 70-84 (1968).
- [54] R.A. Soref, *Interrelation of pyroelectric and nonlinear optical coefficients in ferroelectric crystals*, IEEE J. Quantum Electron. **QE-5**, 126-129 (1969).
- [55] O. Bidault, S. Fossier, J. Mangin, P. Strimer, A. Yelisseyev, L. Isaenko, and S. Lobanov, *Study of the pyroelectricity in LiInS₂ crystal*, Solid State Commun. **121**, 207-211 (2002).
- [56] Ch. Ebberts, *Summary of known nonlinear properties of LiInS₂*, preprint UCRL-ID-116744 Feb. 1994, LLNL, Livermore, USA.
- [57] Yu M. Andreev, L.G. Geiko, P.P. Geiko, S.G. Grechin, *Optical properties of a nonlinear LiInS₂ crystal*, Quantum Electronics **31**, 647-648 (2001) [transl. from Kvantov. Elektronika (Moscow) **31**, 647-648 (2001)].
- [58] Yu M. Andreev, V.V. Badikov, P.P. Geiko, S.G. Grechin, *Fulfillments of phase-matching conditions and optical characteristics of lithium thioindate nonlinear crystals*, Atmospheric and Oceanic Opt. **14**, 1001-1004 (2001) [transl. from Optika Atmosfery i Okeana **14**, 1087-1090 (2001)].
- [59] V. V. Badikov, V.I. Chizhikov, V.V. Efimenko, T.D. Efimenko, V.L. Panyutin, G.S. Shevyrdyaeva, S.I. Scherbakov, *Optical properties of lithium indium selenide*, Opt. Mat. **23**, 575-581 (2003).
- [60] V.G. Dmitriev, D. N. Nikogosyan, *Effective nonlinearity coefficients for three-wave interactions in biaxial crystals of mm2 point group symmetry*, Opt. Commun. **95**, 173-182 (1993).
- [61] K.V. Djesperov, V. G. Dmitriev, *Effective nonlinear coefficient for sum-frequency generation with collinear phase matching calculated taking account of the birefringence in biaxial crystals*, Quantum Electron. **27**, 433-436 (1997) [transl. from Kvantovaya Elektronika **24**, 445-448 (1997)].
- [62] M.V. Hobden, *Phase-matched second-harmonic generation in biaxial crystals*, J. Appl. Phys. **38**, 4365-4372 (1967).
- [63] J.Q. Yao, T.S. Fahlen, *Calculations of optimum phase match parameters for the biaxial crystal KTiOPO₄*, J. Appl. Phys. **55**, 65-68 (1984).
- [64] F. Brehat, B. Wyncke, *Calculation of double-refraction walk-off angle along the phase-matching directions in non-linear biaxial crystals*, J. Phys. B: At. Mol. Opt. Phys. **22**, 1891-1898 (1989).
- [65] J. Yao, W. Sheng, W. Shi, *Accurate calculation of the optimum phase-matching parameters in three-wave interactions with biaxial nonlinear-optical crystals*, J. Opt. Soc. Am. B **9**, 891-902 (1992).
- [66] W. Q. Zhang, *Optical parametric generation for biaxial crystals*, Opt. Commun. **105**, 226-232 (1994).
- [67] V. I. Zadorozhnyi, *Improved analytical method for calculating the parameters of phase-matched nonlinear-optical interactions in biaxial crystals*, Opt. Commun. **176**, 489-501 (2000).
- [68] W.Q. Zhang, *Group-velocity matching in the mixing of*

- three noncollinear phase-matched waves for biaxial crystal, *Opt. Commun.* **221**, 191-197 (2003).
- [69] M. H. van der Moeren, Th. Rasing, H. J. A. Bluyssen, *Determination of the type I phase matching angles and conversion efficiency in KTP*, *Appl. Opt.* **34**, 934-937 (1995).
- [70] F. Rotermund, V. Petrov, F. Noack, V. Pasiskevicius, J. Hellström, F. Laurell, H. Hundertmark, P. Adel, C. Fallnich, *Compact all-diode-pumped femtosecond laser source based on chirped pulse optical parametric amplification in periodically poled KTiOPO₄*, *Electron. Lett.* **38**, 561-563 (2002).
- [71] R. Holzwarth, Th. Udem, T.W. Hänsch, J.C. Knight, W.J. Wadsworth, and P. St. J. Russell, *Optical frequency synthesizer for precision spectroscopy*, *Phys. Rev. Lett.* **85**, 2264-2267 (2000).
- [72] F. Rotermund, V. Petrov, *Femtosecond noncollinear optical parametric amplification in the mid-infrared range with 1.25 μm pumping*, *Jpn. J. Appl. Phys.* **40**, 3195-3200 (2001).
- [73] H. J. Liu, G. F. Chen, W. Zhao, Y. S. Wang, T. Wang, S. H. Zhao, *Phase-matching analysis of noncollinear optical parametric process in nonlinear anisotropic crystals*, *Opt. Commun.* **197**, 507-514 (2001).
- [74] J.-J. Zondy, M. Abed, and A. Clairon, *Type-II frequency doubling at $\lambda = 1.30 \mu\text{m}$ and $\lambda = 2.53 \mu\text{m}$ in flux-grown potassium titanyl phosphate*, *J. Opt. Soc. Am. B* **11**, 2004-2015 (1994).
- [75] R.C. Eckardt, H. Masuda, Y.X. Fan, and R.L. Byer, *Absolute and relative nonlinear optical coefficients of KDP, KD*P, BaB₂O₄, LiIO₃, MgO:LiNbO₃, and KTP measured by phase-matched second-harmonic generation*, *IEEE J. Quantum Electron.* **26**, 922-933 (1990).
- [76] J.-J. Zondy, *Comparative theory of walkoff-limited type-II versus type-I second harmonic generation with Gaussian beams*, *Opt. Commun.* **81**, 427-440 (1991).
- [77] B. Boulanger, J. P. Feve, G. Marnier, C. Bonnin, P. Villeval, J. J. Zondy, *Absolute measurement of quadratic nonlinearities from phase-matched second-harmonic generation in a single KTP crystal cut as a sphere*, *J. Opt. Soc. Am. B* **14**, 1380-1386 (1997).
- [78] J.-J. Zondy, D. Touahri, O. Acef, *Absolute value of the d_{36} nonlinear coefficient of AgGaS₂: prospect for a low-threshold doubly resonant oscillator-based 3:1 frequency divider*, *J. Opt. Soc. Am. B* **14**, 2481-2497 (1997).
- [79] R. A. Kaindl, F. Eickemeyer, M. Woerner, T. Elsaesser, *Broadband phase-matched difference frequency mixing of femtosecond pulses in GaSe: experiment and theory*, *Appl. Phys. Lett.* **75**, 1060-1062 (1999).
- [80] P. Canarelli, Z. Benko, R. Curl, and F.K. Tittel, *Continuous-wave infrared laser spectrometer based on difference frequency generation in AgGaS₂ for high-resolution spectroscopy*, *J. Opt. Soc. Am. B* **9**, 197-202 (1992).
- [81] W. Chen, J. Burie, D. Boucher, *Midinfrared cw difference-frequency generation using a synchronous scanning technique for continuous tuning of the full spectral region from 4.7 to 6.5 μm* , *Rev. Sci. Instrum.* **67**, 3411-3415 (1996).
- [82] D. Lee, T. Kaing, and J.-J. Zondy, *An all-diode-laser-based, dual-cavity AgGaS₂ cw difference-frequency source for the 9–11 μm range*, *Appl. Phys. B* **67**, 363-367 (1998).
- [83] W. Chen, G. Mouret, D. Boucher, *Difference-frequency laser spectroscopy detection of acetylene trace constituent*, *Appl. Phys. B* **67**, 375-378 (1998).
- [84] J.-J. Zondy, *The effects of focusing in type-I and type-II difference-frequency generations*, *Opt. Commun.* **149**, 181-206 (1998).
- [85] A.D. Ludlow, H.M. Nelson, and S.D. Bergeson, *Two-photon absorption in potassium niobate*, *J. Opt. Soc. Am. B* **18**, 1813-1820 (2001).
- [86] L. Isaenko, A. Yelisseyev, S. Lobanov, V. Petrov, F. Rotermund, J.-J. Zondy, G.H.M. Knippels, *LiInS₂: A new nonlinear crystal for the mid-IR*, *Mat. Sci. Semicond. Proc.* **4**, 665-668 (2001).
- [87] H. Mabuchi, E.S. Polzik, and H.J. Kimble, *Blue-light-induced infrared absorption in KNbO₃*, *J. Opt. Soc. Am. B* **11**, 2023-2029 (1994).
- [88] L. Shiv, J.L. Sorensen, and E.S. Polzik, *Inhibited light-induced absorption in KNbO₃*, *Opt. Lett.* **20**, 2270-2272 (1995).
- [89] L. Isaenko, A. Yelisseyev, L. Lobanov, I. Vasilyeva, V. Petrov, V. Nadolinny, J. Smirnova, J.-J. Zondy, *Effect of deviation from stoichiometry on photoinduced absorption in LiInS₂ nonlinear crystals*, Abstract of the 8th European Conf. on Solid State Chemistry (ECSSC-8), 4-7 July, 2001, Oslo, Norway, p. 119 (2001).
- [90] G. C. Catella and D. Burlage, *Crystal growth and optical properties of AgGaS₂ and AgGaSe₂*, *MRS Bulletin / July 1998*, pp. 28-36.
- [91] U. Simon, S. Waltman, I. Loa, F.K. Tittel, and L. Hollberg, *External-cavity difference-frequency source near 3.2 μm based on combining a tunable diode laser with a diode-pumped Nd:YAG laser in AgGaS₂*, *J. Opt. Soc. Am. B* **12**, 323-327 (1995).
- [92] M.A. Acharekar, J.L. Montgomery, and R.J. Rapp, *Laser damage threshold measurements of AgGaSe₂ crystal at 9 μm* , in *Laser-Induced Damage in Optical Materials: 1991*, H.E. Bennett, L.L. Chase, A.H. Guenther, B.E. Newnam, M.J. Soileau, eds., *Proc. SPIE* **1624**, 46-54 (1992).
- [93] A. Harasaki and K. Kato, *New data on the nonlinear optical constant, phase-matching and optical damage of AgGaS₂*, *Jpn. J. Appl. Phys.* **36**, 700-703 (1997).
- [94] B.C. Ziegler and K.L. Schepler, *Transmission and damage-threshold measurements in AgGaSe₂ at 2.1 μm* , *Appl. Opt.* **30**, 5077-5080 (1991).
- [95] Yu. M. Andreev, V. V. Badikov, V. G. Voevodin, L.G. Geiko, P.P. Geiko, M.V. Ivashchenko, A.I. Karapuzikov, I.V. Sherstov, *Radiation resistance of nonlinear crystals at a wavelength of 9.55 μm* , *Quantum Electronics* **31**, 1075-1078 (2001) [transl. From *Kvantov. Elektronika* (Moscow) **31**, 1075-1078 (2001)].
- [96] J. Mangin, G. Jeandel, and G. Marnier, *Temperature dependence of polarization in KTiOPO₄ single crystals*, *Phys. Stat. Sol. A* **117**, 319-323 (1990).
- [97] L. Isaenko, A. Yelisseyev, S. Lobanov, A. Titov, V. Petrov, J.-J. Zondy, P. Krinitsin, A. Merkulov, V. Vedenyapin, J. Smirnova, *Growth and properties of LiGaX₂ (X=S, Se, Te) single crystals for nonlinear optical applications in the mid-IR*, *Cryst. Res. Technol.* **38**, 379-387 (2003).
- [98] S. Zelt, *Fabereicht Physik, Universität Kaiserslautern (Germany)*, personal communication.